Experimental investigations into SGP laminated glass under low velocity impact

Wang, Xing-er; Yang, Jian; Liu, Qiang; Zhao, Chenjun

DOI:
10.1016/j.ijimpeng.2018.06.010

Document Version
Peer reviewed version

Citation for published version (Harvard):
Wang, X, Yang, J, Liu, Q & Zhao, C 2018, 'Experimental investigations into SGP laminated glass under low velocity impact', *International Journal of Impact Engineering*. https://doi.org/10.1016/j.ijimpeng.2018.06.010

Experimental investigations into SGP laminated glass under low velocity impact

Xing-er Wang , Jian Yang , Qiang Liu , Chenjun Zhao

PII: S0734-743X(18)30049-6
DOI: 10.1016/j.ijimpeng.2018.06.010
Reference: IE 3122

To appear in: *International Journal of Impact Engineering*

Received date: 15 January 2018
Revised date: 25 June 2018
Accepted date: 27 June 2018

Please cite this article as: Xing-er Wang , Jian Yang , Qiang Liu , Chenjun Zhao , Experimental investigations into SGP laminated glass under low velocity impact, *International Journal of Impact Engineering* (2018), doi: 10.1016/j.ijimpeng.2018.06.010

Highlights

- Drop weight tests were conducted to investigate the impact damage of SGP laminated glass.
- The high speed camera was adopted to capture the crack initiation and propagation.
- 27 SGP laminated glass panels in eight groups were tested using a mean minimum breakage velocity test approach.
- The effects of panel sizes, interlayer thickness, support conditions and glass make-ups on the impact behaviour were investigated.
- The impact energy and peak impact force that trigger the glass breakage were determined.
- The dynamic stiffness, energy dissipation and delamination behaviour are reported.

Experimental investigations into SGP laminated glass under low velocity impact

Xing-er Wang[a,b], Jian Yang[a,b,c], Qiang Liu[d], Chenjun Zhao[a,b]

[a] State Key Laboratory of Ocean Engineering, School of Naval Architecture, Ocean and Civil Engineering, Shanghai Jiao Tong University, Shanghai 200240, PR China

[b] Collaborative Innovation Center for Advanced Ship and Deep-Sea Exploration (CISSE), Shanghai 200240, P.R. China

[c] School of Civil Engineering, University of Birmingham, Birmingham B15 2TT, UK

[d] China Academy of Building Research (CABR), Beijing, 100013, PR China

Abstract: The structural use of laminated glass (LG) is growing rapidly. To meet safety and post-breakage strength requirements, a SentryGlas®Plus (SGP) interlayer has been widely used in LG. Limited data has been available to date concerning the impact resistance of SGP LG. This paper describes an experimental investigation into the damage behaviour of SGP LG panels under hard-body impact. A mean minimum breakage velocity (MMBV) test approach has been employed to determine the breakage energy. By tracing the crack initiation through the use of high speed filming, six categories of breakage sequence have been classified. The characteristics of crack propagation, including the lagging time between the initiation of different cracks and the typical crack propagation speed, were also obtained. This is followed by the identification of the representative cracking morphology and the motion behaviour of the impactor. The impact resistance of SGP LG has been calculated by examining the effects of the design variables such as the LG panel size, interlayer thickness, the support conditions and the glass make-up. It was found that the influence of LG panel size on the MMBV and both pre- and post-breakage stiffness is limited, and increasing the interlayer thickness cannot improve the resistance to glass breakage under impact. The LG panel with clamped edges requires more MMBV to trigger glass breakage and has an increase of 44% in pre-breakage stiffness compared to the panel with bolted connections at four corners. The evident improvement in post-breakage stiffness due to the beneficial fragmentation pattern of heat strengthened (HS) glass, compared to its counterpart of

fully tempered (FT) glass, has also been revealed. However, the differences in MMBV between them are modest. Results also indicate that a significant degradation of dynamic stiffness in the post-breakage stage can be found in both the double layered LG with thicker interlayer, and in the triple layered LG. The energy dissipation behaviours were also examined, and results suggest that the energy dissipation ratio can be greater than 40% in most instances, and the thicker interlayer will produce negative effects on dissipating impact energy. Two types of delamination are identified, and the dependency of their delamination growth on the impact velocity is analysed.

Keywords: Laminated glass; Impact; SGP Interlayer; Structural glass; Dynamic load; Delamination

1. Introduction

Laminated glass (LG) is widely adopted in glass façade construction and the automotive industry, and has been dominated in the last few decades by the use of a polyvinyl butyral (PVB) interlayer. Laminated glass has also found a novel application as a load bearing component in recent times. However, the residual static load carrying capacity and stiffness of PVB laminated glass is known to be limited after glass breakage [1]. A novel polymer, SentryGlas®Plus (SGP) [2], having higher stiffness and strength than PVB, has been developed to offer better post-breakage strength and thus is recommended for use in structural applications. Due to the brittleness of the glass layer, both PVB and SGP laminated glass present significant vulnerability when subjected to dynamic load, such as windborne debris [3-5], head impact [6] and blast load [7-9].

The windborne debris generated in severe windstorms can lead to serious threats to the laminated glass often used in building envelopes. Following the specifications introduced by the design codes and standards, e.g. ASTM E1886 [10] and E1996 [11], small size steel balls [12, 13] and large size wooden blocks [14] have been chosen by several researchers to represent windborne hard and soft projectiles, respectively. Laminated glass panels consisting of annealed (AN) glass layers with dimensions of 0.2 m × 0.2 m were tested using 1.8 - 2.2 gram granite chipping with an impact velocity in the range of 4 - 20 $m \cdot s^{-1}$ [15]. The results showed that the critical velocity for triggering damage depended strongly on the thickness of outmost glass layer. A change in the fracture mode from star cracking to cone cracking as the overall laminate thickness increased was identified as well. Behr [16] investigated the dynamic strains on the inner glass layer of three LG make-ups under 2 gram steel ball impact, in which the impact speed varied from 9.1 $m \cdot s^{-1}$ to 21.3 $m \cdot s^{-1}$. The peak strain agreed well with the analytical finite element model proposed. It was found that the peak radial strain was unaffected as PVB thickness increased. Large scale tests of laminated glass under impact of small missiles weighing 2 to 28.2 gram were also reported [17], in which samples sized 1.52 m × 1.83 m and 0.61 m × 0.61 m were used. A mean minimum breakage velocity (MMBV) for breaking the inner glass layer was determined. The order of importance for design variables influencing the impact resistance of LG was also established, indicating that the inner glass layer type and thickness were the dominant factors. Zhang [14] tested annealed glass windows subjected to large size wooden block impact, with impact velocity varying from 9 $m \cdot s^{-1}$

to 35 $m \cdot s^{-1}$. The interlayer thickness was found to dominate the penetration resistance capacity. The vulnerability curve of LG windows with various thicknesses and dimensions were also proposed to assess the window performance under wood debris impact.

In contrast to windborne debris, the impactor involved in car accidents is usually the head of a pedestrian. The head is proposed by the European Enhanced Vehicle-Safety Committee (EEVC) to be modelled as an aluminium sphere covered by a PVC skin, which weighs approximately 5 kg [18]. Pyttel [19] conducted a series of headform impact tests with both curved and plane laminated glass, in which the impact velocity was set from 5 $m \cdot s^{-1}$ to 12 $m \cdot s^{-1}$. A failure criterion based on the concept of critical energy threshold was subsequently proposed for finite element simulations. Liu [20] carried out a set of tests on real car windscreens under headform impact at velocities ranging from 6.6 $m \cdot s^{-1}$ to 11.2 $m \cdot s^{-1}$ and at impact angles ranging from 60° to 90°. The evaluation of the peak contact force and head injury criterion (HIC) demonstrated the correlation between the PVB interlayer properties and the energy absorption capability of the windscreen. The glass failure and tensile deformation of the PVB interlayer were found to have a coupled contribution to the HIC value, whereas the Young's modulus and yield stress of the interlayer presented negligible effects on both peak contact force and HIC.

However, the above impact tests concentrated on PVB laminated glass and a limited range of glass make-ups and support systems. For instance, the samples tested were commonly two glass layers, which were both annealed (AN), heat strengthened (HS) and fully tempered (FT) glass, but combinations of different glass types were not considered. The samples were set to be simply supported [21, 22] or clamped [23], whereas bolted connections which are frequently employed in glass façade construction were ignored. No results concerning the impact damage of SGP laminated glass have been reported so far. Most research regarding this type of laminated glass focuses on the static behavior [24-26].

The purpose of this investigation is to study experimentally the impact performance of SGP laminated glass panels subjected to low velocity impact from a hard impactor. An experimental rig was first erected to accommodate different support conditions such as edge clamping and bolt fixing. A series of drop weight impact tests on SGP laminated glass panels was then performed. The testing regime was designed to capture the breakage energy following a mean minimum breakage velocity (MMBV) concept. The LG specimens tested in this study included two typical

dimensions, i.e. 1000 × 1000 mm and 1500 × 1500 mm, with a variety of glass make-ups comprising double or triple HS and FT glass layers, and various thicknesses of the SGP interlayer. By analyzing the crack initiation captured with high speed filming, the breakage sequences are established and classified into six categories. The crack propagation speeds are also determined. A thorough analysis of the crack patterns and the motion behavior of the impactor prior to and after breakage are also carried out. The effects of the design variables on the impact behavior, e.g. the minimum breakage energy, dynamic stiffness and energy absorption performance, are examined. Two types of delamination are identified and the dependency of their delamination growth on the impact velocity is analysed.

2. Laboratory tests

2.1 Testing apparatus

The typical application scenarios of SGP laminated glass as load bearing members can be seen in pedestrian bridges or floor slabs, where glass is often subjected to an out of plane load. Impact action often occurs when a pedestrian drops an object or furniture falls over. In addition, windborne debris, e.g. tiles or broken glass pieces, will also impart similar action on glass walls. Design codes and specifications suggest that a hard projectile can be modelled as a 2 g steel ball (ASTM E1996 [11]) for windborne debris and a 4.11 kg steel ball (BS EN 356 [27]) for vandal attack. However, in the structural application, the impact scenarios are often greater than these two cases, e.g., furniture collapse. In this study, the impactor was designed to be a 13.5 kg weight with a spherical head of 40 mm radius and a cylindrical body. A high capacity integrated circuit piezoelectric (ICP) force sensor was placed between the head and the impactor body to measure the impact force.

Figure 1 shows the impact testing apparatus. It consists of a guide pipe up to 6 m high and a specially designed steel platform, which was fabricated to provide the supports for clamped or bolted connections for different specimen dimensions. A high-speed camera (12,500 frames per second with a resolution of 1024 × 1024 pixels) with two spotlights was used to record the impact process of the specimens via a mirror placed underneath the specimen. The high-speed camera

recording was triggered when the transformed voltage from the RF1 accelerometer glued to the inner surface of the LG panel (see **Fig. 1**) exceeded the specified value (nearly 2.2 V). It is worth noting that the RF1 was 80 mm away from the panel centre instead of being located centrally beneath the impact point. This is because if sensors are glued exactly beneath the point of impact debonding will always occur, even if a high performance adhesive is used. All sensors were connected to data acquisition units with multiple modules. A sampling frequency of 100 kHz was adopted during the tests.

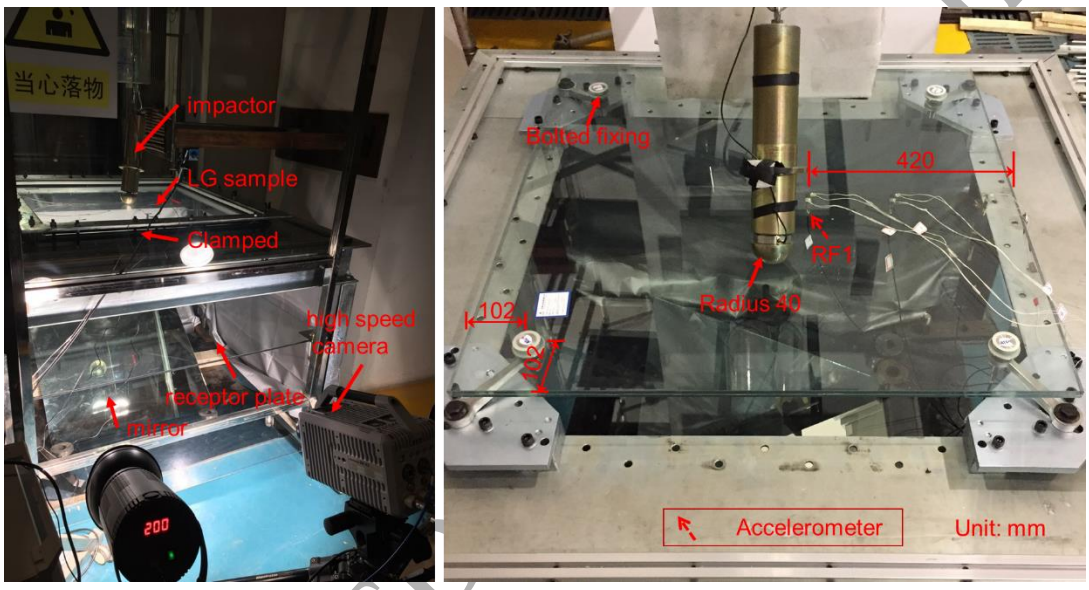

Fig. 1. The drop-weight testing apparatus.

2.2 Testing specimens

In this study, 27 SGP laminated glass specimens in eight groups (See **Table 1**) were selected for testing. Several identical laminated glass panels were tested within each group. Five design variables such as the LG panel size, glass type, interlayer thickness, the support conditions and the glass make-up were investigated. Heat strengthened (HS) and fully tempered (FT) glass were employed and combined to make different types of laminated glass. The specimens were 1000 mm × 1000 mm or 1500 mm × 1500 mm in size, with each glass panel being 8 mm thick. The SGP interlayer thickness varied from 3 mm to 5 mm. As shown in **Fig. 2 (a)**, seven groups of specimens were fixed with bolts to the testing platform using four countersunk bolts. Another

group (No. 8) was fully clamped by clamping frames around all sides (**Fig. 2 (b)**). Neoprene gaskets were placed between the aluminum frame and the LG specimen.

Table 1 SGP laminated glass configurations tested under impact

ID No.	LG configuration	Thickness (mm)	Support system	Dimensions (mm × mm)	Specimen number	Variable investigated
1	FT/S/FT	8/3/8	Bolted	1000 × 1000	6	Glass type
2	FT/S/FT	8/3/8	Bolted	1500 × 1500	3	Dimension
3	HS/S/FT	8/3/8	Bolted	1000 × 1000	3	Glass type
4	FT/S/FT	8/5/8	Bolted	1000 × 1000	3	Interlayer thickness
5	FT/S/FT/S/FT	8/3/8/3/8	Bolted	1000 × 1000	3	Glass make-up
6	HS/S/HS/S/FT	8/3/8/3/8	Bolted	1000 × 1000	3	Glass make-up
7	HS/S/FT/S/FT	8/3/8/3/8	Bolted	1000 × 1000	3	Glass make-up
8	FT/S/FT/S/FT	8/3/8/3/8	Clamped	1000 × 1000	3	Boundary condition

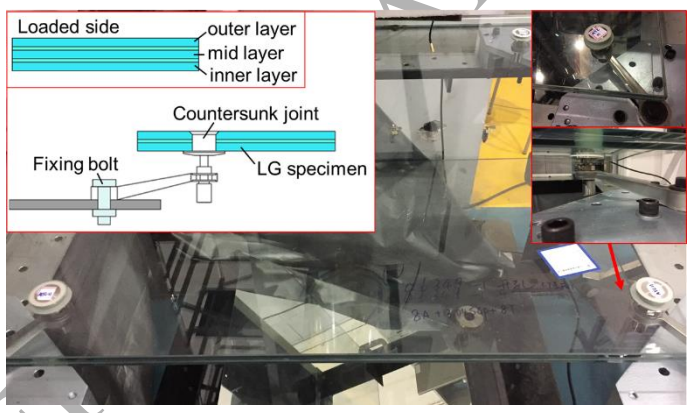

(a) Bolted fixing using countersunk joint

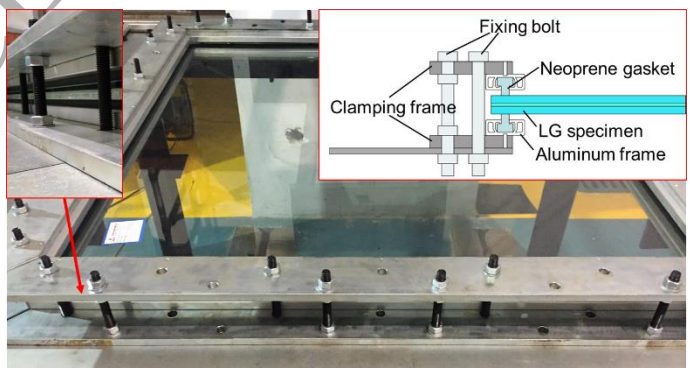

(b) Clamping frame

Fig. 2. Schematic illustration of support systems.

A mean minimum breakage velocity (MMBV) test procedure [17] was employed in this study to capture the impact resistance for each type of SGP LG specimen. The MMBV approach is characterised by a series of impact tests with gradually increasing drop height until all glass layers break. The initial drop height between the impactor tip and the LG outer surface was based on a rough evaluation of the impact breakage energy, and each test specimen was intended to have several impact attempts before the first constituent glass panel started to break. Following the initial impact height, the drop height was increased in increments of 0.2 m. After the first constituent glass panel was broken, the drop height was reduced to a level of 0.4 m lower than that resulting in the first breakage of the glass layer. The specimen was tested three times at its initial drop height.

3 Experimental results

3.1 Overview

3.1.1 Breakage sequence and crack propagation

The breakage sequence of each specimen is classified into six categories based on experimental observations, which are:

1) BS1: outer^{1}-inner^{2}, 2) BS2: inner^{1}-outer^{2} and 3) BS3: inner^{1} & outer^{1}, for double glass layered specimens; and 4) BS4: outer^{1}-mid^{2}-inner^{3}, 5) BS5: outer^{1}-mid^{2} & inner^{2} and 6) BS6: outer^{1}-inner^{2}-mid^{3}, for triple glass layered specimens. In the above category descriptions, the superscript represents the breaking order, e.g., BS3 means that both inner and outer glass layers break simultaneously. The post-breakage stage is after the first glass breakage occurs. In order to accurately establish the breaking order of BS3 and BS5, the high speed filming results were reviewed to precisely locate their crack initiation instances which were indistinguishable by the naked eye. Meanwhile, the features of their crack propagation were identified.

High speed photos of specimens No. 1 and No. 5, having BS3 and BS5 type of breakage sequence respectively, are shown in **Fig. 3**. The cracking fronts were located to obtain the mean crack propagation speed, with each frame having an interval of 0.08 ms. The front edges of the radial cracks and the rippled cracks are denoted by the yellow dot-dashed and green dashed circles,

respectively. The time of the crack initiation is found to be 0.08 ms after the high speed camera was triggered.

It can be found from **Fig. 3 (a)** that the radial cracks in specimen No. 1 initiate in the inner glass layer. The radial cracks are caused by the tensile stress waves in the circumferential direction on the bottom surface. The rippled cracks subsequently originate from the impact point with a lagging time of 0.96 ms. The rippled cracks are caused by the progressive fracture of glass due to the internal stress release of the fully tempered glass, which is triggered by the crack initiation resulting from the large contact force. The shorter lagging time of 0.08 ms between the radial and the rippled cracks in specimen No. 5 is shown in **Fig. 3 (b)**.

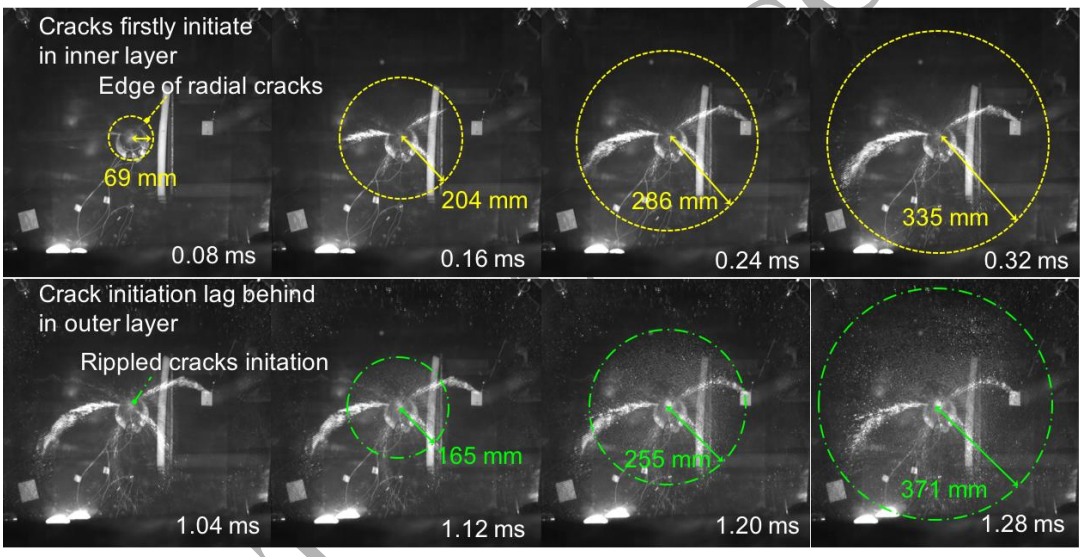

(a) Specimen No. 1(BS3) at impact velocity of 3.3 m·s^{-1}.

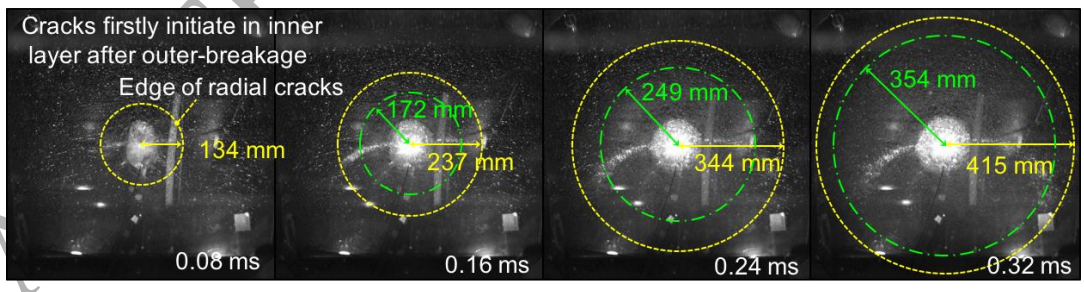

(b) Specimen No. 5 (BS5) at impact velocity of 4.5 m·s^{-1}.

Fig. 3. Typical crack initiation and propagation of specimens No. 1 (BS3) and No. 5 (BS5).

The crack propagation speed obtained for the specimens in **Fig. 3** is summarised and shown in **Fig. 4**. It can be seen that the propagation speed of rippled cracks in both cases show the same

trend, i.e. deceleration first and then acceleration. The peak speed of rippled cracks in the BS5 case (around 2146 m·s^{-1}) is slightly greater than that in the BS3 case (around 2063 m·s^{-1}). **Figure 4** also shows that the propagation speed of the radial cracks is evidently lower than that of the rippled cracks, with a peak speed of approximately 1688 m·s^{-1} in BS3 and 1335 m·s^{-1} in BS5. The propagation speed of radial cracks in BS3 experiences a monotonic decline, the crack tip propagation decelerates to nearly 600 m·s^{-1} when it reaches the edge. In comparison to the monotonic trend in BS3, the radial crack tip in BS5 first accelerates to 1335 m·s^{-1} and then decelerates to 890 m·s^{-1} afterwards. A similar observation on the propagation of the radial cracks can be found [28], where its trend and peak can be traced within 0.04 ms after the crack initiation. Therefore, one can anticipate that the propagation speed of radial cracks up to 0.08 ms in BS3 may also show the same trend but there is no evidence to support this argument due to an absence of high speed photos.

Through analysing the high speed photos, it can be summarized that both radial and rippled cracks propagate to the panel edge between 0.32 ms and 0.40 ms. From this, it indicates that the mean crack propagation speed is more than 1250 m·s^{-1}, but less than 1563 m·s^{-1}. Such results are close to the theoretical approximation [29] and other experimental observations [30, 31].

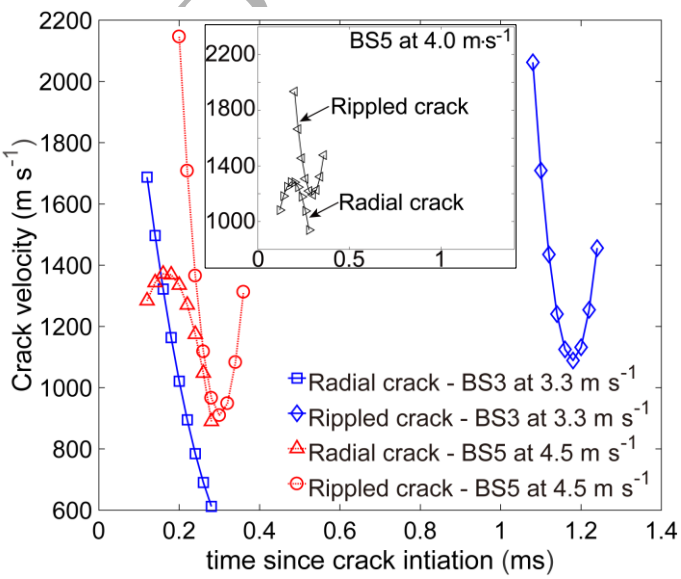

Fig. 4. Crack propagation speed of specimens No. 1 (BS3) and No. 5 (BS5)

In addition, **Figure 4** shows an inset figure that presents the crack propagation speed in BS5 when impact velocity decreases to 4.0 m·s^{-1}. It should be noted that the case in BS3 with a

different breakage velocity from 3.3 m·s^{-1} cannot be found in the same glass make-up and is hence not included in **Fig. 4**. Compared with the results at the impact velocity of 4.5 m·s^{-1}, the peak propagation speeds of both radial (around 1933 m·s^{-1}) and rippled cracks (around 1280 m·s^{-1}) at the impact velocity of 4.0 m·s^{-1} have an evident decrease. However, both cases show a similar variation pattern. Such observation supports the conclusion that the peak propagation speed is expected to decline when impact velocity decreases. As the crack propagation is driven by the stress component normal to the crack front [32], which can be significantly reduced by decreasing impact velocity.

3.1.2 Crack pattern

As mentioned above, the typical crack patterns observed in the experiment are rippled cracks and radial cracks. In addition, different glass types present significant differences in the local crack patterns near the impact point. As shown in **Fig. 5 (a)**, the outer glass layer of No. 3 which is HS glass, exhibits a core cracked zone comprising several large petal shaped fragments. A circular crack along the edge of the petal shaped fragments can be observed and acts as a boundary dividing the core cracked zone and the rippled crack zone. Large HS glass fragments can be observed in the rippled crack zone. In contrast, the crack pattern in the inner layer appears to be mostly in the radial

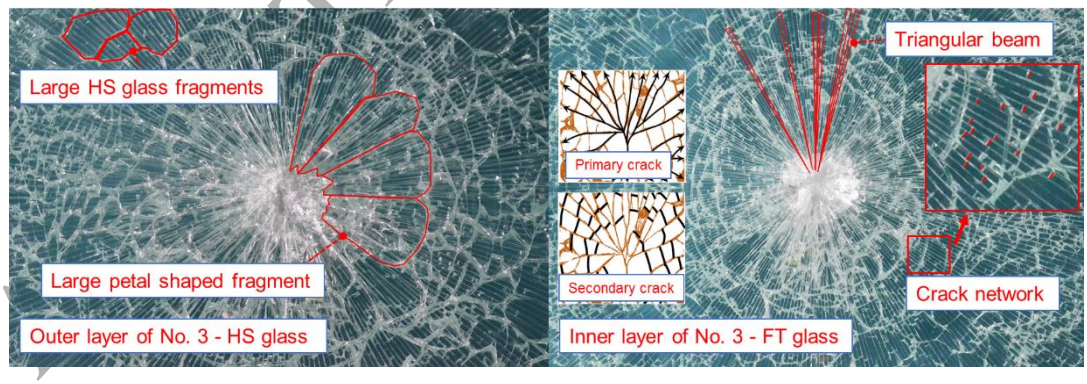

(a) Crack patterns of HS/S/FT

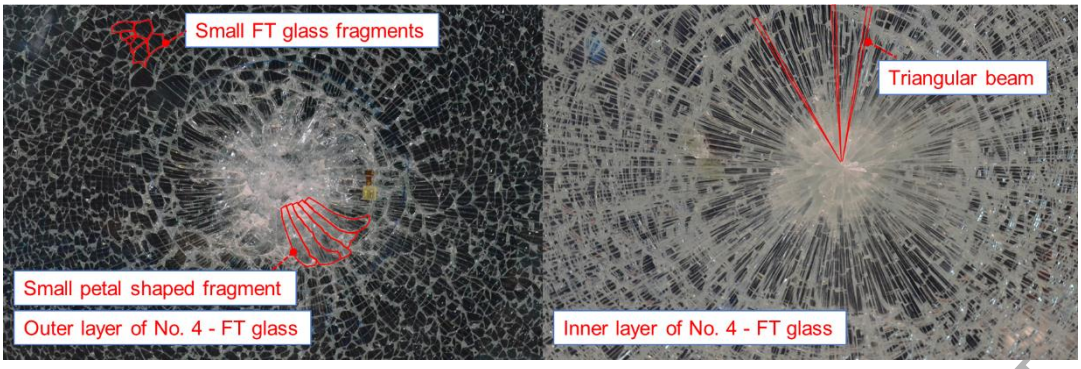

(b) Crack patterns FT/S/FT glass.

Fig. 5. Typical crack patterns of LG specimens tested.

direction and in the form of shard-shaped triangular beams. Like crack patterns that have previously been reported [33], the cracks in the triangular beams include: 1) primary cracks which are outgoing radial cracks, 2) secondary cracks, i.e. a crack network cutting off the different triangular beams, which is driven by the redistribution of the residual stress field.

Figure 5 (b, left) shows the crack pattern of the outer FT glass layer, which presents a smaller core cracked zone comprising small petal shaped fragments. The petal shaped fracture of FT glass propagates with a tendency to become skewed. This is different from the HS glass case where the outward cracks of a petal shaped fracture are almost perfectly radial with larger fragments. This agrees with the typical fragment patterns of HS and FT glass under static loads. As predicted, small FT glass fragments can be observed outside the core cracked zone.

3.1.3 Impactor motion

The impactor motion in specimen No. 4 where both glass layers break simultaneously is considered. The acceleration and displacement history is plotted in **Fig. 6**, where the impact velocity of 2.9 $m \cdot s^{-1}$ represents the case of glass being intact, and the impact velocity of 3.1 $m \cdot s^{-1}$ being the breakage case. According to the impact response in the breakage case, the entire impact process can be divided into three stages.

Stage 1 (0-0.8 ms) is designated as “glass breakage stage”. It can be seen that the impact duration in the elastic case is approximately 2 ms, and in the breakage case it is approximately 0.8 ms. The oscillation of the acceleration curve is due to the dynamic coupling effect between impactor and glass panel. Such coupling effect can be frequently seen in the hard body impact [34].

It may be caused by the interaction between the local deformation behavior of glass and the impactor movement. The sudden decrease of acceleration in Stage 1 in the breaking case indicates the instant of glass breakage.

Stage 2 (0.8-18 ms) can be categorised by the large deformation of the broken glass panel and continuing downward movement of the impactor, and so is referred to as the "large deformation stage". The impactor velocity decreases to zero, with the displacement reaching a maximum of nearly 17 mm in this example. As mentioned, the cracks propagate to the panel edge in less than 0.5 ms, which suggests most cracks were formed during Stage 2. The peak acceleration in Stage 2 decreases to 85 g and presents a plateau afterwards, showing that the impactor keeps in contact with the glass panel. In the elastic case in Stage 2, a second peak of acceleration can be found at 5.2 ms. Note that the acceleration declines to zero at 6.0 ms and the displacement drops to zero at 5.6 ms, i.e., marking the moment when the impactor separates from the glass surface, and then when it bounces above the original glass level, respectively.

Stage 3 (18-50 ms) is defined as the "rebounding stage" because the impactor starts to bounce back from its location of maximum displacement. It can be seen that the impactor remains separated from the cracked glass panel during the time interval of 21.2-28.2 ms. The impactor is then hit again by the vibrating glass panel at 28.2 ms, so that the acceleration subsequently presents another oscillation behaviour followed by a smooth plateau. The SGP interlayer still acts elastically in this stage and maintains the capability of holding the cracked glass panel together.

When compared with the impact motion of the PVB LG panel that has previously been reported [20], the impactor acceleration for the SGP LG panel exhibits more rapid variation so that its first plateau ends at nearly 21.2 ms, while that of PVB LG ends at later than 60 ms. The peak impactor displacement of the PVB LG is approximately 90 mm. Such peak displacement is much larger than that of SGP LG, which is 17 mm, which can be attributed to the greater stiffness of the SGP interlayer.

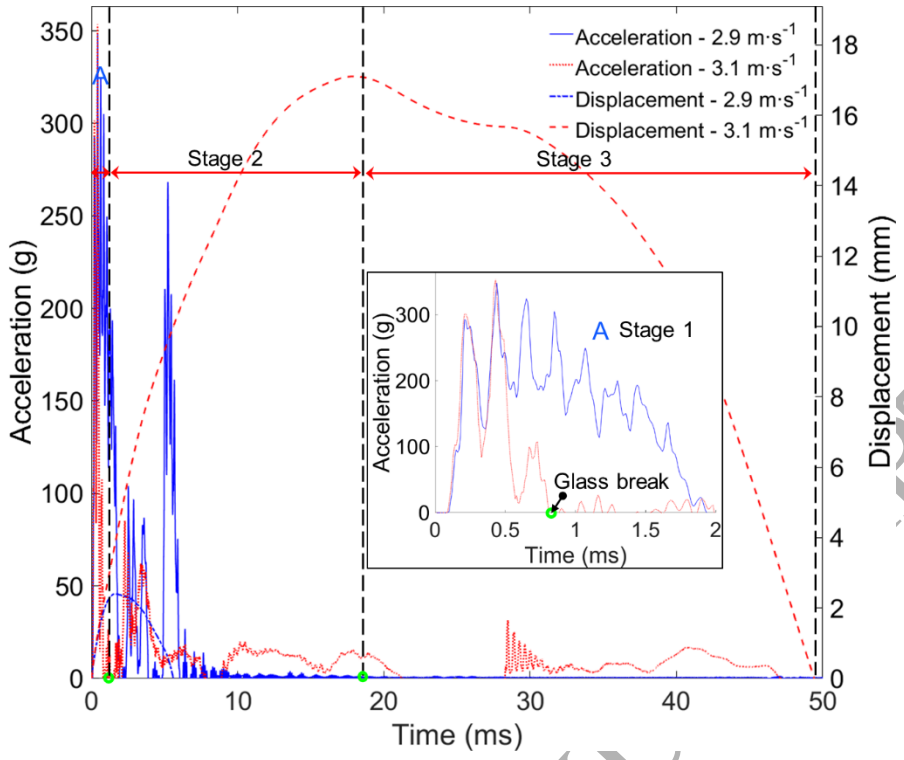

Fig. 6. Typical impactor motion at various impact velocities.

3.2 Breakage velocity and breakage stiffness

The mean value and standard deviation of the breakage velocity v_{break} that triggers the breakage of glass, and the ratio of the peak impact force P_{max} to the maximum deflection w_{max} defined as the breakage stiffness, β_k, at the breakage of each layer, are recorded and summarised in **Table 2** for the double layered specimens, and **Table 3** for the triple layered specimens.

In the case of the double layered specimens, it is noted that β_k in BS2 is significantly lower than that in BS1 at the first breakage. It is shown that the breakage stiffness for the specimens with the first breakage occurring in the inner layers is approximately 66% lower than that of the specimens first breaking in the outer layers. The cracked outer layer in BS1 can withstand compression and thus continue contributing stiffness. In contrast, the cracked inner layer in BS2 cannot sustain tension, leaving only the interlayer carrying tension, resulting in significant stiffness degradation. The β_k of No.1 group in BS3 is not available because of an accidental signal malfunction, so that the stiffness degradation in BS3 cannot be compared with that in BS1 and BS2. However, it can still be predicted by analysing β_k of the remaining specimens in BS3 that the breakage stiffness is nearly 15% of that in BS1 at the first breakage, and is slightly higher than that in BS1 at the second breakage.

In examining the effect of specimen size, it can be found that the breakage stiffness of specimen No. 2 (1500 × 1500 mm) is slightly lower than that of the smaller specimens with the same glass make-up, i.e. the No. 1 group, at the first breakage, but it is negligibly higher at the second breakage. It is also found that the impact velocity required to cause the breakage of the No. 2 group is close to that of the No. 1 group. This suggests that the influence of specimen size on both the breakage energy and dynamic stiffness is limited.

By comparing β_k of the No. 4 and No. 1 groups in BS1, it can be seen that the stiffness has an increase of 6% at the first breakage, and an increase of 13% at the second breakage, when the thickness of the SGP interlayer varies from 3 mm in the No. 1 group to 5 mm in the No. 4 group. However, the breakage velocity remains unchanged or exhibits a slight decrease when the interlayer thickness becomes greater. This indicates that increasing the interlayer thickness is not particularly effective in enhancing the impact resistance.

Unlike the other glass configurations, the No. 3 group, comprising the hybrid glass type, i.e. HS and FT glass, shows the same breakage sequence, with both layers breaking at the same impact. This type of breakage sequence is undesirable because it can only withstand reduced impact energy after the breakage of first panel.

Table 2 Breakage sequence and impact response of double layered specimens

Breakage sequence	ID No.	1st breakage				
		v_{break} (m·s^{-1})	v_{break} (m·s^{-1}) (mean ± std)	P_{max} (kN)	w_{max} (mm)	β_k (kN·mm^{-1}) (mean ± std)
BS1	1	2.5	2.6 ± 0.2	39.5	2.38	18.3 ± 1.2
		2.9		50.3	2.60	
		2.5		41.6	2.18	
	2	2.7	2.7	41.0	2.43	16.9
	4	2.9	2.6 ± 0.3	46.8	2.36	19.4 ± 0.4
		2.3		35.1	1.84	
BS2	1	4.5	3.5 ± 1.0	68.8	10.54	6.2 ± 0.3
		2.5		42.5	7.18	
BS3	1	3.3	3.3	N/A	N/A	N/A
	2	3.3	3.3 ± 0.0	49.3	19.64	2.5 ± 0.0
		3.3		47.1	18.90	
	3	2.7	2.8 ± 0.1	42.6	12.57	3.0 ± 0.4
		2.7		39.4	12.90	
		2.9		40.3	16.23	
	4	3.1	3.1	46.8	17.10	2.7

				2nd breakage		
BS1	1	3.1	3.2 ± 0.1	36.8	17.73	1.5 ± 0.5
		3.3		21.6	28.06	
		3.3		33.4	22.32	
	2	3.1	3.1	39.3	15.68	2.5
	4	3.3	3.1 ± 0.2	34.4	17.70	1.7 ± 0.2
		2.9		26.5	18.32	
BS2	1	5.9	4.2 ± 1.7	58.0	36.22	1.9 ± 0.3
		2.5		26.5	12.37	

It can be seen in **Table 3** below that the breakage stiffness of the triple layered specimens are significantly higher than those of the double layered specimens. The specimens in BS5 present higher stiffness than those in BS4 at the first breakage. In the BS4 and BS5 cases, the outermost glass layers both break first. Compared to the BS4 case, the No.5 and No. 7 groups in BS5 reveals higher impact resistance at the second breakage, and whereas the impact resistance of the No.6 group in BS5 has a slight decrease.

Table 3 Breakage sequence and impact response of triple layered specimens

Breakage sequence	ID No.	1st breakage				
		v_{break} (m·s^{-1})	v_{break} (m·s^{-1}) (mean ± std)	P_{max} (kN)	w_{max} (mm)	β_k (kN·mm^{-1}) (mean ± std)
BS4	5	1.9	1.9	39.8	1.16	34.4
	6	2.3	2.1 ± 0.2	57.1	1.25	37.7 ± 8.0
		1.9		37.1	1.25	
	7	1.9	1.9	40.2	1.25	32.0
	8	2.3	2.5 ± 0.2	55.0	1.22	49.4 ± 4.4
		2.7		73.9	1.37	
BS5	5	2.5	2.4 ± 0.1	64.4	1.27	51.2 ± 0.6
		2.3		62.1	1.20	
	6	2.3	2.3	58.6	1.24	47.3
	7	2.3	2.2 ± 0.1	57.6	1.25	41.8 ± 4.3
		2.1		45.5	1.21	
BS6	8	2.5	2.5	65.6	1.26	52.3
				2nd breakage		
BS4	5	2.9	2.9	51.5	2.07	24.9
	6	3.3	2.9 ± 0.4	60.6	2.23	32.9 ± 5.7
		2.5		54.4	1.41	
	7	2.5	2.5	55.6	1.49	37.3
	8	4.0	4.5 ± 0.5	63.7	3.62	14.6 ± 3.0
		4.9		65.5	5.62	

BS5	5	4.0	4.2 ± 0.2	61.4	10.16	5.4 ± 0.7
		4.5		60	12.71	
	6	2.7	2.7	62.7	6.52	9.6
	7	2.9	3.3 ± 0.4	65.6	7.35	6.9 ± 2.1
		3.8		71.2	14.88	
BS6	8	4.7	4.7	75.7	3.67	20.6
				3rd breakage		
BS4	5	3.1	3.1	30.8	8.31	3.7
	6	3.3	3.1 ± 0.2	27.0	15.06	4.5 ± 2.7
		2.9		46.4	6.45	
	7	2.9	2.9	43.1	7.16	6.0
	8	3.5	3.8 ± 0.2	25.6	14.08	3.2 ± 1.4
		4.0		28.4	6.11	
BS6	8	3.8	3.8	47.3	8.95	5.3

The No. 8 group specimens with the clamped edges obtain apparently lower post-breakage stiffness than the No. 5 group specimens with corners fixed by bolts, as evidenced by a decrease in stiffness of 41% at the second breakage and a decrease of 14% at the third breakage, while the pre-breakage stiffness (at the first breakage) was 44% higher in the No. 8 group than in the No. 5 group. The table also shows that a higher impact velocity is required to break the No. 8 group than that needed to break the No. 5 group specimens, as expected. It can also be observed from specimen No. 8 that the breakage sequence has no strong correlation to the breakage velocity. Table 3 reveals that BS6 has the highest stiffness at each breakage.

An increase of the post-breakage stiffness (that at the second breakage) can be found in the specimens containing the HS glass compared to those entirely made up of FT glass layers, in both BS4 and BS5. This may be caused by the beneficial cracking pattern of larger HS glass fragments.

3.3 Peak impact force and breakage energy

An overview of breakage energy and associated peak impact force, P_{max} is shown in **Fig. 7**. It can be seen that in laminated glass higher impact energy is required to generate the subsequent breakage (e.g. second or third breakage) than the preceding one. The No. 5 and No. 7 groups have one more fully tempered glass layer than the No. 1 and No. 3 groups. Comparing the impact energy causing the first breakage, one can see that the triple layered specimens are more vulnerable to impact breakage. The mean breakage energy in the triple layered specimens (≤ 38 J)

has a considerable decrease from the double layered specimens (≥ 46 J). This is due to the higher stiffness resulting in difficulty in dissipating impact energy through elastic deformation. This reveals that in the glass design, adding the glass layer has a detrimental effect on the impact resistance. For instance, the breakage energy causing the initial breakage of the outer glass layer of the No. 5 group, (which contains three FT glass layers), is only 53% of that of the No. 1 group, (which consists of two FT glass layers) in BS4; and is 85% of that of the No. 1 group in BS5.

As **Fig. 7 (b)** shows, a significant increase in breakage energy can be seen in the post-breakage stage of the No. 5 group in BS5 compared with the specimens with HS glass layers, i.e., the No. 6 and No. 7 groups. It can be seen that the No. 5 group with three FT glass layers presents the highest breakage energy, followed by the No. 7 group with two FT glass layers, while that of the No. 6 group with only one FT glass layer ranks the lowest. Such results can satisfactorily confirm the prediction that the glass type will dominate the post-breakage energy in BS5.

From **Fig. 7 (a)**, a similar conclusion can be made when comparing the first breakage energy of the No. 1 and 3 groups in BS3. Specimen No. 1, with two FT glass layers, requires more impact energy to trigger the simultaneous failure of both glass layers than specimen No. 3, with one FT glass layer.

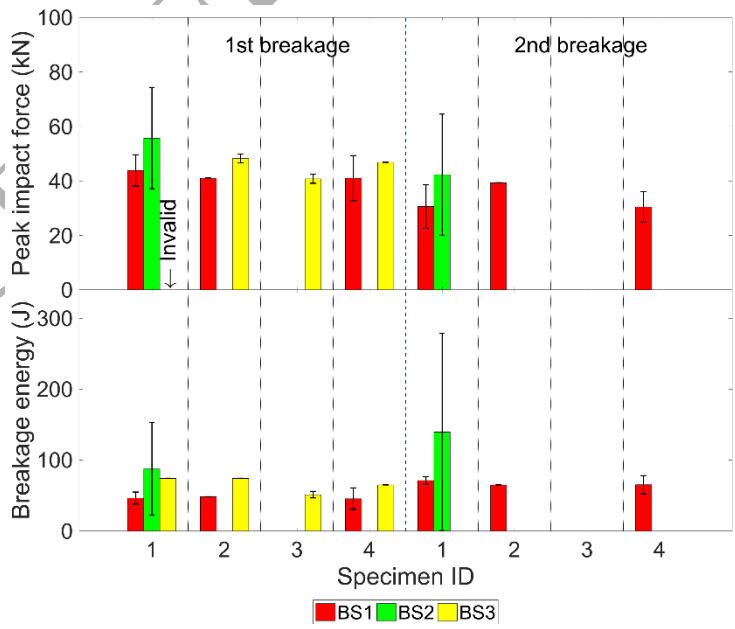

(a) Double layered specimens

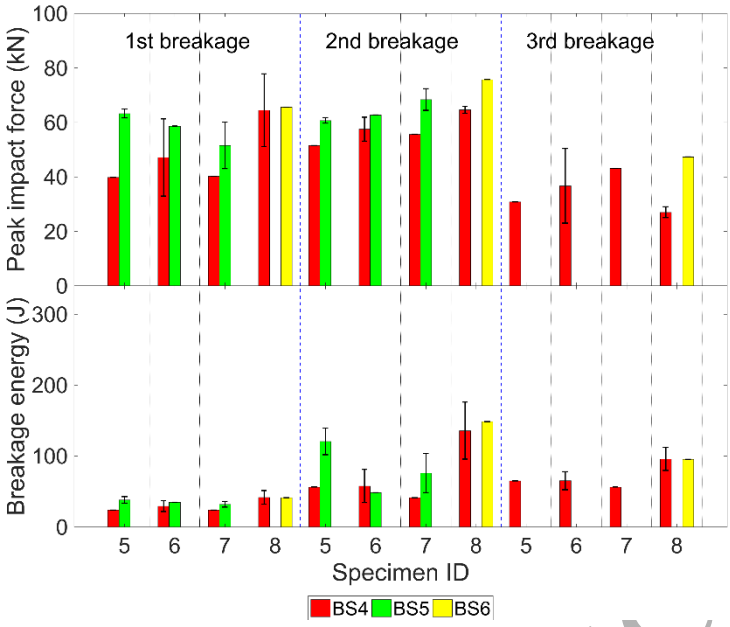

(b) Triple layered specimens

Fig. 7. Breakage energy and peak impact force of SGP LG specimens.

It can also be seen in **Fig. 7 (a)** that No. 2 and 4 specimens break at a similar energy level. This agrees with the previous observation that the influence on the breakage energy of a change in SGP interlayer thickness and specimen size is negligible, both in the pre- and post-breakage stages. Unexpectedly, the specimens with clamped edge supports tend to be harder to break than those with bolted fixings, especially in the post-breakage stage.

Figure 7 (b) shows that the No.8 specimens have higher breakage energy levels than the No. 5 specimens. As previously discussed, the lower post breakage stiffness of the No.8 specimens (see **Table 3**) leads to lower contact force, so that higher breakage energy is required.

Figure 7 (b) reveals that the peak impact force at the second breakage is larger than that at the first breakage; e.g. for specimen No. 7 in BS4 a 29% increase in peak impact force can be seen, and in BS5 there is a 38% increase. The peak impact force at the third breakage is demonstrated to be the lowest on most occasions, with the reduction ratio reaching 22% in the No. 5 (bolted fixing) group, and 58% in the No. 8 group (edge clamped), when compared to that at the first breakage. At the third breakage, the tension is sustained by the SGP interlayer at the moment that all glass layers fail. The lower Young's modulus of SGP interlayer (around 0.3 GPa) than the glass layer (around 70 GPa) leads to the largest deflection and greatest impactor contact time, so that the impact force appears to be the lowest. Likewise, in the double layered specimens, a 30% reduction in the peak impact force can be seen in the No. 1 group at the second breakage in **Fig. 7 (a)**.

The influence on peak impact force of the interlocking mechanism from various glass fragment types can also be examined. The interlocking mechanism refers to interactive action under compression between the neighboring glass fragments, which will render different global response of broken LG panel. For instance, the HS glass fragments have larger size and favorable fragmentation pattern than the FT glass fragments as evidenced by the higher stiffness. The outer and mid glass layers break in BS4 after the second breakage occurs. It can be seen in Fig. 7 (b) that, after the second breakage occurs in BS4, the No. 6 specimen containing two HS cracked layers (outer and mid layers) experiences the highest peak impact force P_{max}, while for specimen No. 7, with one HS layer and one FT layer cracked, there is a decrease in P_{max}. Specimen No. 5, with two FT cracked layers, achieves the lowest P_{max}. Such a trend correlates well with that of the breakage stiffness and confirms the significant effect of the interlocking mechanism of glass fragments under compression. It is worth noting that in **Fig. 7 (b)** the mean P_{max} at the third breakage in the No. 6 group is lower than that in the No. 7 group, which does not entirely agree with the previous conclusion. However, a large standard deviation in P_{max} of the No. 6 specimen is also observed. Therefore, it is reasonable to expect that such a reduction may be caused by one odd result amongst the repeated tests.

3.4 Impact force versus impact velocity

During the repeated impact attempts between two consecutive breakages, the energy balance model can be adopted to analyse the impact dynamics of SGP LG specimens. The relationship between the peak impact force, P_{max} and the impact velocity can then be obtained using the energy balance model. If the effects of membrane and local deformation are omitted, the relationship can be simply written as follows [35]:

$$P_{max} = (K_{bs}M)^{1/2}V \quad (1)$$

where V represents the impact velocity, K_{bs} is the linear stiffness including bending and transverse shear deformation effects, and M is the projectile mass. It can be seen that the P_{max} will increase linearly with the projectile velocity if the linear stiffness K_{bs} remains unchanged. In order to examine the potential stiffness degradation caused by the accumulated damage of glass and interlayer prior to the glass layer breaking, the results of peak impact force versus the impact

velocity of double layered and triple layered specimens are recorded and shown in **Fig. 8** and **Fig. 9**, respectively. **Fig. 8 (a)** to **Fig. 8 (d)** refer to the results of No. 1 to No. 4 configurations, respectively. **Fig. 9 (a)** to **Fig. 9 (d)** refer to the results of No. 5 to No. 8 configurations, respectively.

Linear or quadratic regression equations are used to fit the data and are presented in the figures. The linear regression shows no significant trend of degradation. The slope is denoted by K in the linear fitting and the slopes of the quadratic lines at both the start and the end points are shown in the figures as K_i and K_e, respectively. It is noting that a large spread of data can be seen in several cases such as No. 1 in BS1 (**Fig. 8 (a1)**), No. 4 in BS1 (**Fig. 8 (d1)**) and No. 8 in BS4 (**Fig. 9 (d1)**). In these cases, it can be seen that the curve fitting to the recorded data is poor in the post breakage stage. In the post breakage stage, the coefficient of determination, R^2, of No. 1 in BS1, No. 4 in BS1 and No. 8 in BS4 are 0.69, 0.5 and 0.6, respectively. Results show great scatter in these cases. This is due to the different damage scales at the contact point in the same group when subjected to consecutive impacts. A more severe cracking will result in the lower impact force. A relatively small R^2 value will thus be more frequently found in the post breakage stage, particularly when the outer glass layer breaks first. Nevertheless, trendiness can still present a correlation between the impact force and impact velocity. In the remaining testing groups, the curve fitting are found to be satisfactory. For instance, in the post breakage stage, R^2 values of No. 1 in BS2, No. 6 in BS4 and No. 7 in BS5 are 0.97, 0.98 and 0.95, respectively. It is worth noting that the internal defects of LG specimens, which will affect the accumulated damage of glass, may be altered by different manufacturers. Such difference will consequently lead to a slight change of the resulting curve fits if more LG specimens are tested.

As shown in **Fig. 8**, the pre-breakage regression line of the double layered specimens is linear in most cases except the No. 4 group (**Fig. 8 (d)**), where obvious nonlinearity can be observed when the impact velocity is greater than 2.5 $m \cdot s^{-1}$. This implies that for the 3 mm thick SGP interlayer, the glass stiffness remains constant until breakage. However, when SGP thickness increases to 5 mm, there occurs some stiffness reduction while the impact velocity approaches the breakage velocity in BS3. This trend is more obvious in the post-breakage stage of BS1 (**Fig. 8 (d1)**).

Comparing specimens No. 1 (**Fig. 8 (a1)**) and 2 (**Fig. 8 (b1)**) in BS1, a 25% reduction in

slope in the pre- breakage stage, and an 8% reduction in slope in the post-breakage stage is observed as the specimen dimensions increase from 1000 × 1000 mm to 1500 × 1500 mm. A greater reduction in slope, of approximately 32 % in the pre-breakage stage, can be seen when the interlayer thickness increases to 5 mm when comparing specimen No.s 1 (**Fig. 8 (a1)**) and 4 (**Fig. 8 (d1)**).

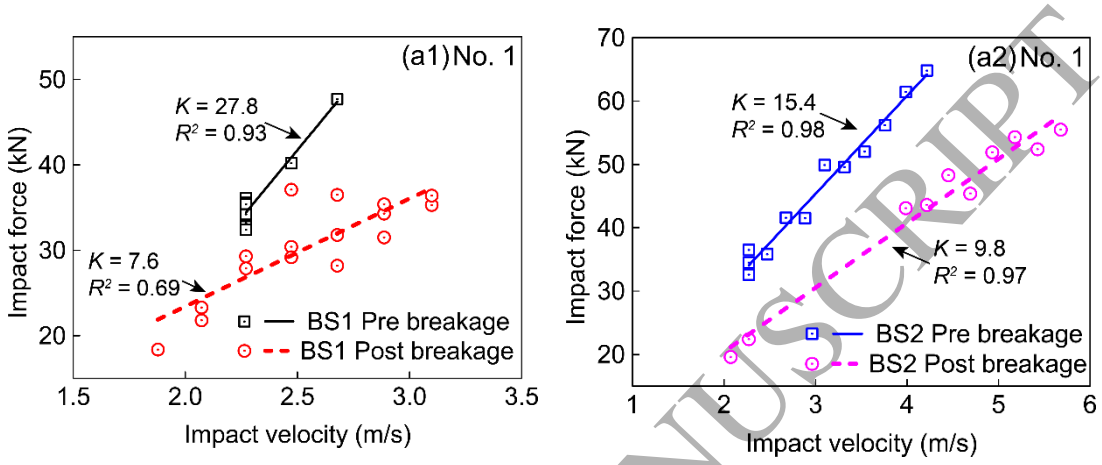

(a) No. 1 group in BS1 and BS2

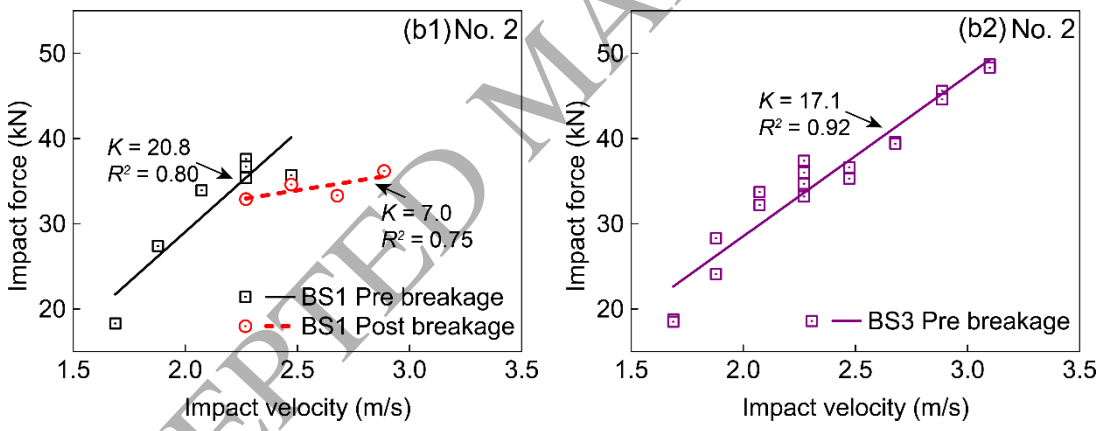

(b) No. 2 group in BS1 and BS3

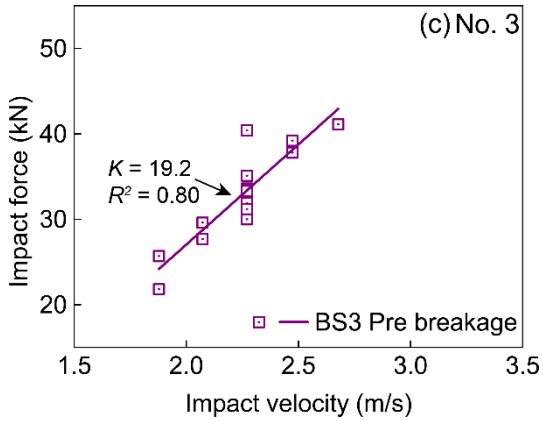

(c) No. 3 group in BS3

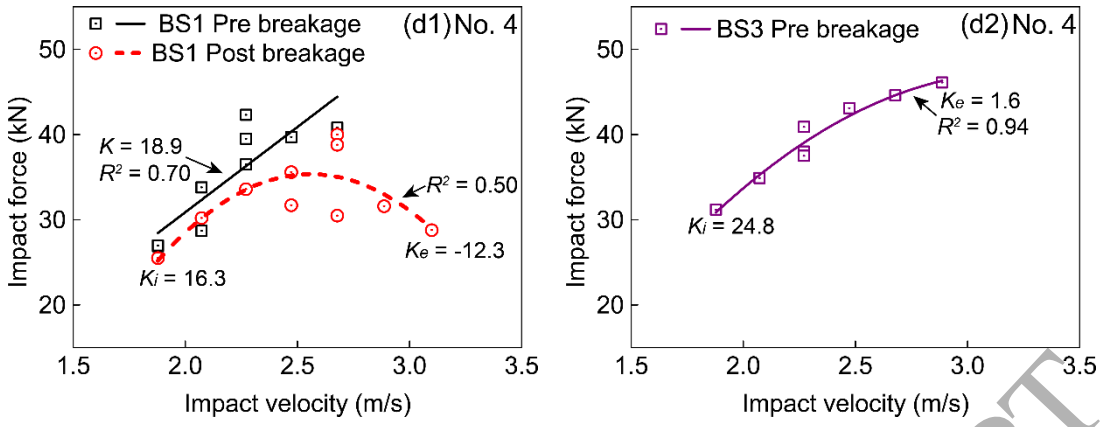

(d) No. 4 group in BS1 and BS3

Fig. 8. Peak impact force versus impact velocity in double layered specimens.

For specimens No. 2 and 4, **Fig. 8** shows that the *K* values in the pre-breakage for BS1 (**Fig. 8 (b1, d1**) and BS3 (**Fig. 8 (b2, d2**) are close in each case. Specimen No. 1 shows a large discrepancy between the *K* values in the pre-breakage BS1 (**Fig. 8 (a1)**) and BS2 (**Fig. 8 (a2)**), which are 27.8 and 15.4, respectively. However, the *K* values in the post-breakage for both BS1 and BS2 are 7.6 and 9.8, respectively. Further investigation can be carried out to examine the relationship between the *K* value and the breakage sequence of laminated glass, which may lead to a potential approach to predict the breakage sequence by applying several non-destructive impacts.

For the No. 5 (**Fig. 9 (a1)**) and No. 7 (**Fig. 9 (c1)**) groups shown in **Fig. 9**, there is an absence of data in the pre-breakage stage. This is because there were not many attempts before the glass breakage occurred. Only the post outer-breakage stage (i.e. after the outer layer breaks) in these two groups are presented. The regression lines in the No. 6 (**Fig. 9 (b1)**) and No. 7 (**Fig. 9 (c2)**) groups exhibit obvious nonlinearity in the post outer-breakage stage. As shown in **Fig. 9**, common trends for all the specimens can be observed: the impact force in the pre-breakage stage remains proportional to the impact velocity in the triple layered specimens; and an evident decline in the *K* value can be seen in the final post breakage stage. Nearly identical *K* values can be found for both the No. 6 (**Fig. 9 (b1, b2)**) and No. 8 groups (**Fig. 9 (d1, d2)**) in the pre-breakage stage, indicating a good consistency in the dynamic stiffness of the triple layered specimens in the pre-breakage stage. Thus, a rational assumption of the pre-breakage stiffness for specimens No. 5 and No. 7 can be made in the breakage sequence of BS4.

The *K* value of the final breakage stage for the No. 5 group in BS4 (**Fig. 9 (a1)**), i.e. post outer-mid-breakage, shows a remarkable decrease of 78% compared to the pre-breakage stage, and 73% compared to the post outer-breakage stage. Similarly, a decreased ratio can be found in the No. 7 group (**Fig. 9 (c1)**), in which the *K* value of the post outer-mid-breakage stage experiences an 80% reduction compared to the pre breakage stage, and a 73% reduction compared to the post outer-breakage stage. In contrast to the high decreasing ratio in BS4, the *K* value of the No. 8 group in the final breakage stage in BS6 (**Fig. 9 (d2)**) presents only a 36% decrease. The above comparison implies that in the case of both outer and middle layers breaking, the LG panel will possess low stiffness, while when only the middle layer is intact, the LG panel still has reasonably high dynamic stiffness.

Figure 9 shows that the dynamic stiffness of the LG panels with HS glass layers, i.e. the No. 6 (**Fig. 9 (b1)**) and No. 7 (**Fig. 9 (c2)**) groups, enters a rapid declining phase when approaching the breakage velocity at approximately 3.0 - 3.5 $m \cdot s^{-1}$ when the mid-glass layer breaks suddenly. In contrast, the LG panels made entirely of FT glass layers, i.e. the No. 5 (**Fig. 9 (a2)**) and No. 8 (**Fig. 9 (d1)**) groups, present a prolonged declining phase until the mid-glass layer breaks at nearly 4.0 - 5.0 $m \cdot s^{-1}$. This indicates that the triple layered LG panels comprising FT glass layers are characterised as having better 'ductility' in the post outer-breakage stage under impact, compared to those hybrid glass panels containing HS glass layers. As shown with specimen No. 8, the dynamic stiffness of edge clamped panels remains almost stable when subjected to increasing impact velocity, showing a slight decline in the *K* value.

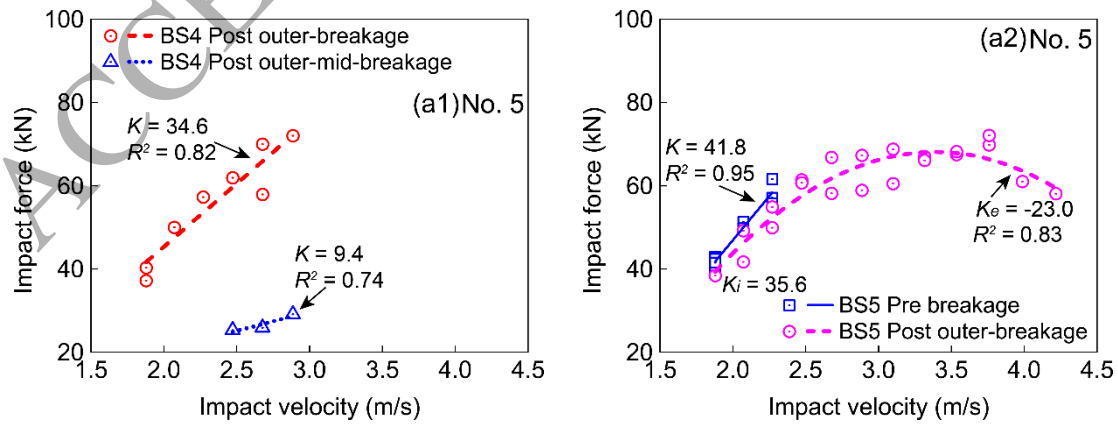

(a) No. 5 group in BS4 and BS5

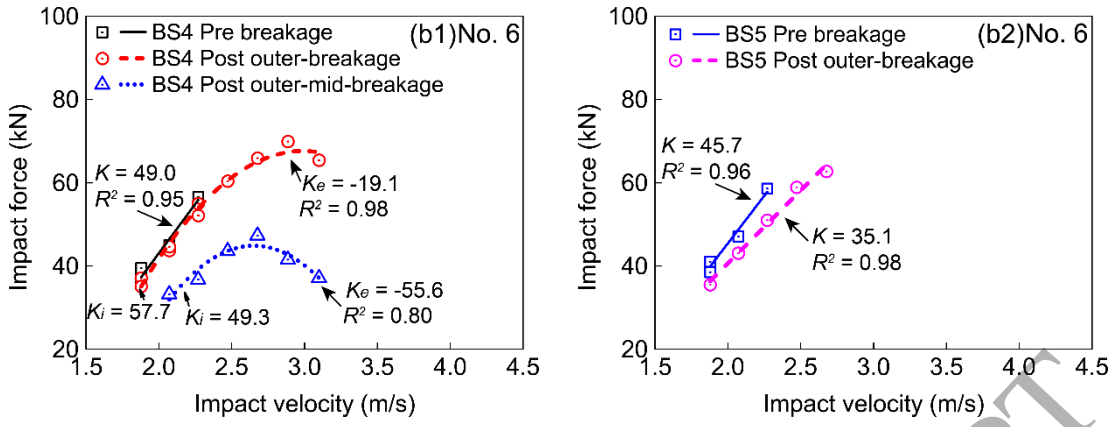

(b) No. 6 group in BS4 and BS5

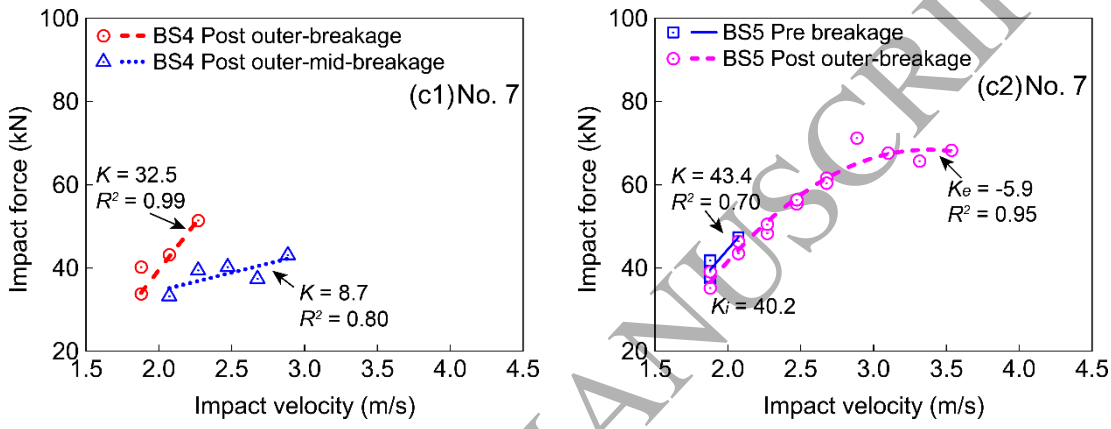

(c) No. 7 group in BS4 and BS5

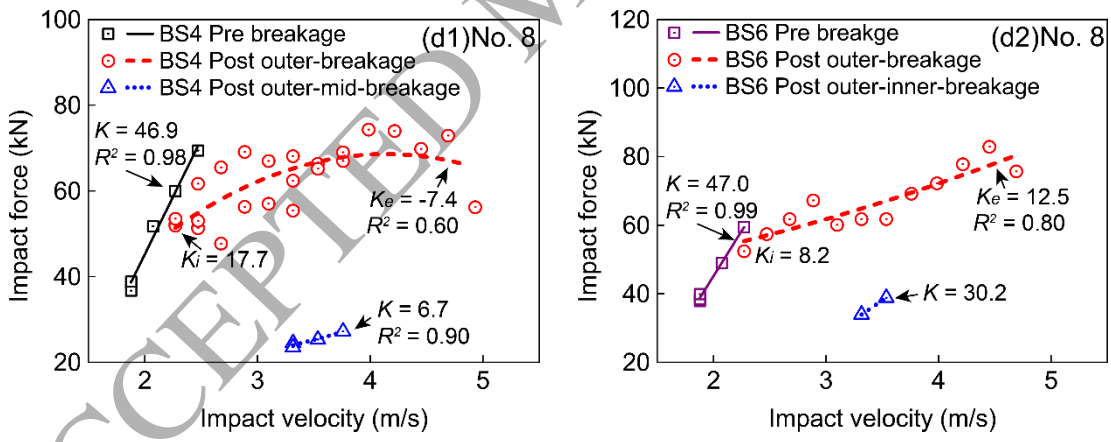

(d) No. 8 group in BS4 and BS6

Fig. 9. Peak impact force versus impact velocity in triple layered specimens.

3.5 Energy dissipation behaviour

The energy dissipated during the impact process and the corresponding energy dissipation ratios of double layered specimens are shown in **Fig. 10,** and of triple layered specimens are

shown in **Fig. 12**. **Fig. 10 (a)** to **Fig. 10 (d)** refer to the results of No. 1 to No. 4 configurations, respectively. **Fig. 12 (a)** to **Fig. 12 (d)** refer to the results of No. 5 to No. 8 configurations, respectively. Quadratic polynomials are used to fit the result data. The energy dissipated, $E_d = E_i - E_r$, and the dissipation ratio, $\beta = 1 - E_r / E_i$ are defined by assuming the energy is balanced in the system consisting of the impactor and the LG panel, where E_i represents the impact energy and E_r denotes the kinetic energy of the rebounding impactor. It is worth noting that a difficulty arises in obtaining accurate energy dissipation characteristics at breakage, because the release of the prestress in the HS and FT glass at breakage leads to a sudden drop in the inherent strain energy. It is unlikely to precisely determine the released energy at breakage and thus the energy balance of the system is disturbed. An example of inaccurate energy dissipation at breakage using the above approach are identified and marked with a red dashed circle in **Fig. 10 (a2)**. The result presents an evident drop in E_d, because the measured rebounding kinetic energy of the impactor, E_r also includes some energy imparted from the prestress released due to the glass cracking, leading to an underestimate of energy dissipation.

It can be seen in **Fig. 10** that the energy dissipation in all the double layered specimens having a BS1 and BS3 breakage sequence is less than 45 J in the elastic stage. The specimens with a HS glass layer (**Fig. 10 (c)**) or thicker SGP interlayer (**Fig. 10 (d1, d2)**) present a declining trend of energy dissipation ratio as the impact velocity increases, varying from nearly 90 % at 1.7 $m \cdot s^{-1}$ to 18 % at 3 $m \cdot s^{-1}$. It is found that a negative effect may be imposed on the energy dissipation ratio when the interlayer thickness increases to 5 mm in the No. 4 group, for which the ratio declines more rapidly than for the No. 2 (**Fig. 10 (b1, b2)**) and No. 3 (**Fig. 10 (c)**) groups when increasing the impact velocity. The negative effect of thicker interlayer on the energy dissipation further indicates that the glass is more likely to accumulate the impact damage in the No. 4 group. Such damage accumulation by thicker interlayer even causes the declining trend of P_{max} - V curve as shown in the Fig. 8 (d1). Moreover, the energy dissipation in No. 4 is the lowest in the double layered specimens. This group presents a descending trend that is different from the other groups, where most results have an ascending trend regardless of the breakage sequence, except for No. 2 in BS1 (**Fig. 10 (b1)**) that behaves in a non-monotonic fashion. This again indicates that a thicker interlayer can have a negative effect on dissipating energy. Unlike the monotonic descending trend, the energy dissipation ratio in specimen No. 1 (**Fig. 10 (a1)**) presents an ascending branch after

reaching its minimum, close to the first breakage velocity as shown in **Fig. 10**.

The behaviour of specimen No. 2 in BS1, as shown in **Fig. 10 (b1)**, indicates that the energy dissipation of No. 2 experiences a non-monotonic trend with an inflexion point near the impact velocity of 2.5 $m \cdot s^{-1}$. Such a trend consists of a peak in the pre-breakage stage and a trough in the post-breakage stage. Only one specimen presents this particular trend and it may be caused by an unusually strong adhesion between the glass and the interlayer. Strong adhesion tends to lead to the outer glass layer and the SGP interlayer having greater local strain and a higher strain rate, and thus the breakage of the outer glass layer is more likely to be triggered [36]. This assumption can be validated by comparing the crack patterns of the two No. 2 specimens broken in different sequences as shown in **Fig. 11**. It can be seen that the outer glass layer of the specimen in BS3 shatters into 'dice' of similar size, while the area near the impact point cracks into large fragments in a 'starburst' pattern (**Fig. 11 (a)**). In contrast, the outer glass layer of the specimen in BS1 shatters into large glass fragments of irregular shape (**Fig. 11 (b)**). Such irregular shapes are probably due to the stronger adhesion between the glass and interlayer. Once one of the FT glass layers breaks, the intact glass holds the broken counterpart through adhesive shear action so that the locked-in stress can be released slowly. In contrast, weak adhesion does not provide such interaction, and thus the glass breaks into a typical fragmentation pattern, namely small 'dice'.

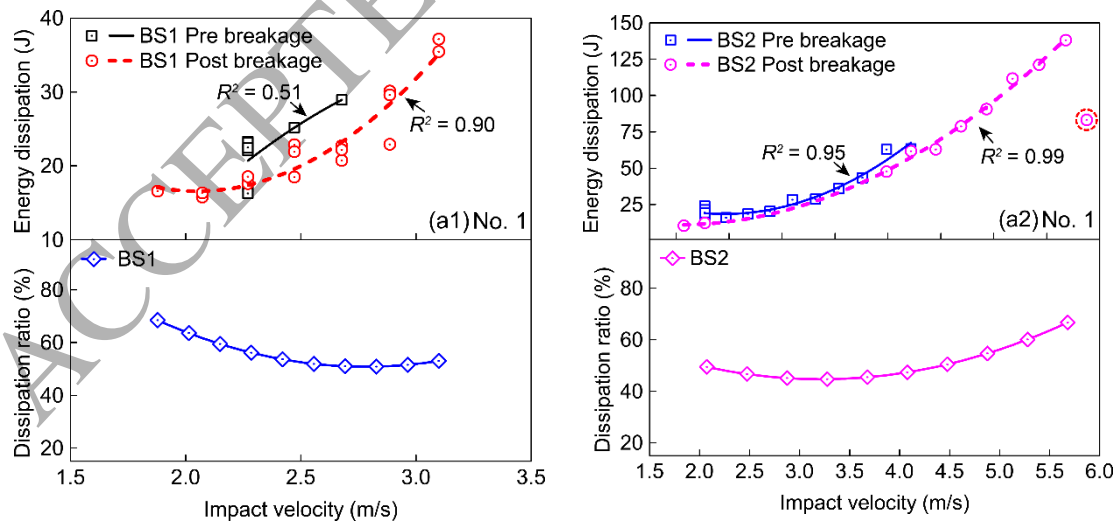

(a) No. 1 group in BS1 and BS2

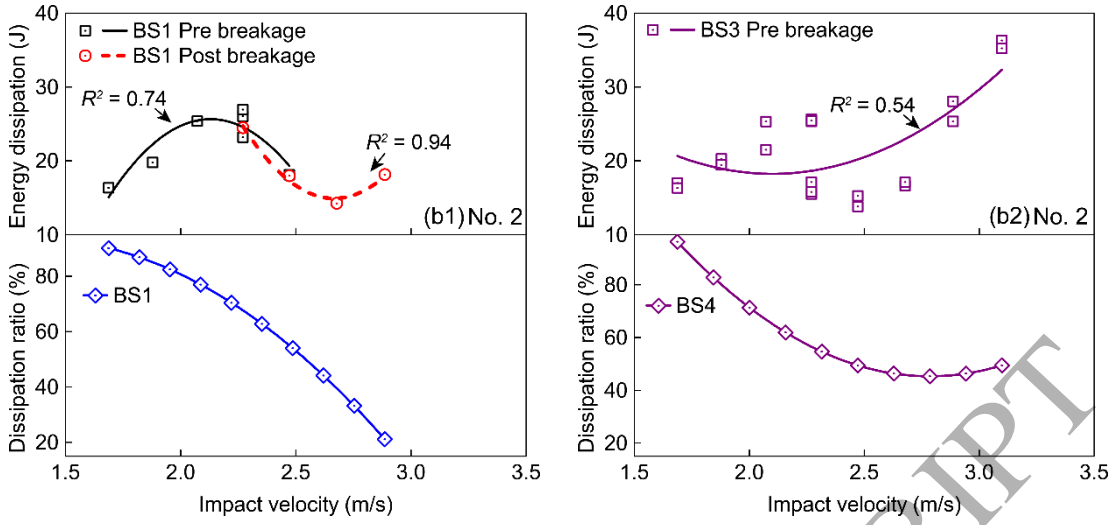

(b) No. 2 group in BS1 and BS3

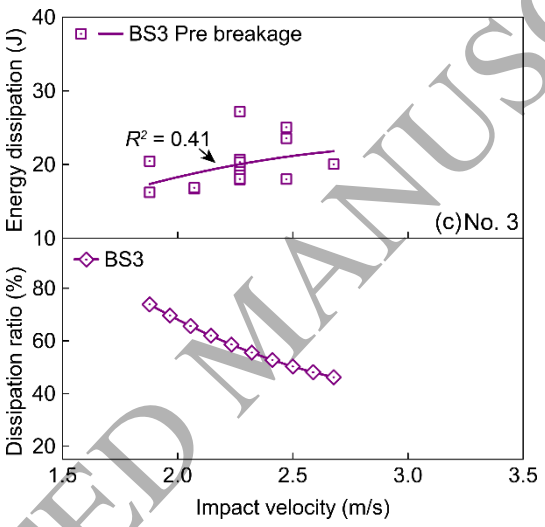

(c) No. 3 group in BS3

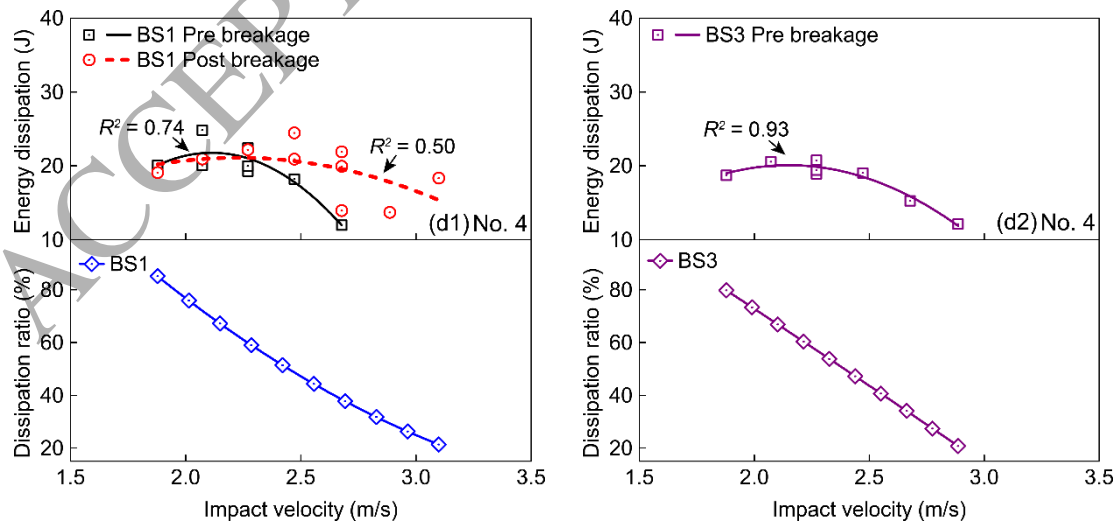

(d) No. 4 group in BS1 and BS3

Fig. 10. Impact energy dissipation and dissipation ratio variation of double layered specimens.

(a) Two glass crack patterns in BS3 at 1st breakage (b) Outer glass crack pattern in BS1 at 1st breakage

Fig. 11. Crack patterns of specimen No. 2 at first breakage.

As shown in **Fig. 12**, a monotonic ascending trend of energy dissipation as the impact velocity increases can be observed in all triple layered specimens. In the case of the No. 8 group (**Fig. 12 (d1, d2)**), a consistent trend of energy dissipation as well as a similar energy dissipation ratio is obtained in different breakage sequences. This indicates that the energy dissipation behaviour of the No. 8 group (edge clamped) is likely to be independent of the breakage sequence. In addition, specimen No. 8 obtains the highest energy dissipation, at approximately 120 J, among the triple layered specimens.

Conversely, the No. 6 group (**Fig. 12 (b)**) achieves the lowest energy dissipation, at less than 45 J. The energy dissipation ratio of specimen No. 6 in BS4 (**Fig. 12 (b1)**) presents a monotonic decreasing trend and achieves a minimum value of 55%. Specimen No. 6 in BS5 (**Fig. 12 (b2)**) reaches a similar level of energy dissipation ratio, occurring at the impact velocity of 2.3m/s. Comparing the energy dissipation of No. 5, No. 6 and No. 7 groups, the highest energy dissipation increases when more FT glass layers are used in making the laminated glass. This indicates that a glass make-up comprising more FT glass layers has a higher capability in dissipating impact energy.

Comparing the energy dissipation ratios of No. 5 (**Fig. 12 (a)**) and No. 7 (**Fig. 12 (c)**) groups, it can be seen that the energy dissipation ratio in all cases will experience an increase when approaching the breakage velocity. The energy dissipation ratio in both groups of BS5 (**Fig. 12 (a2, c2)**) shows a modest variation as compared to BS4 (**Fig. 12 (a1, c1)**).

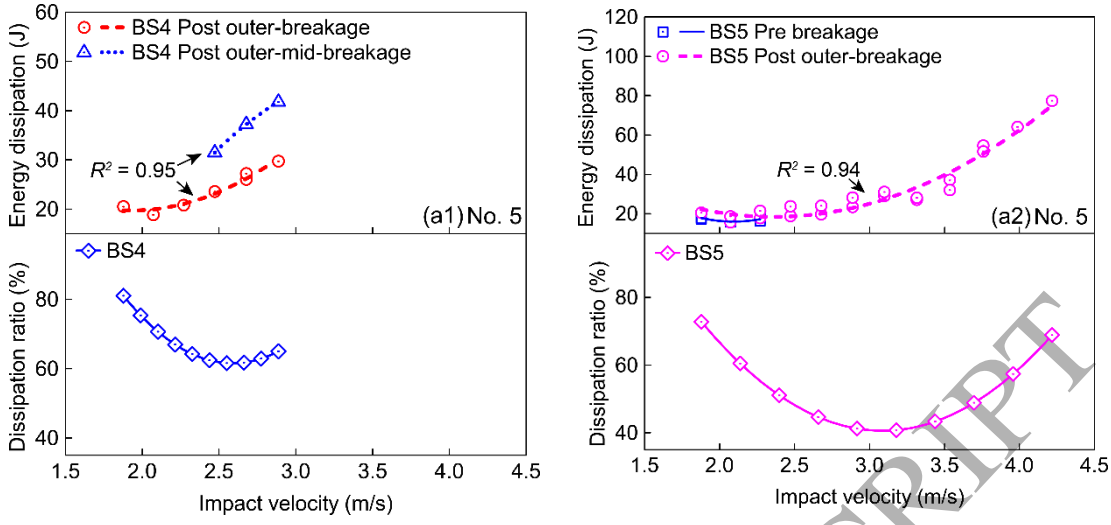

(a) No. 5 group in BS4 and BS5

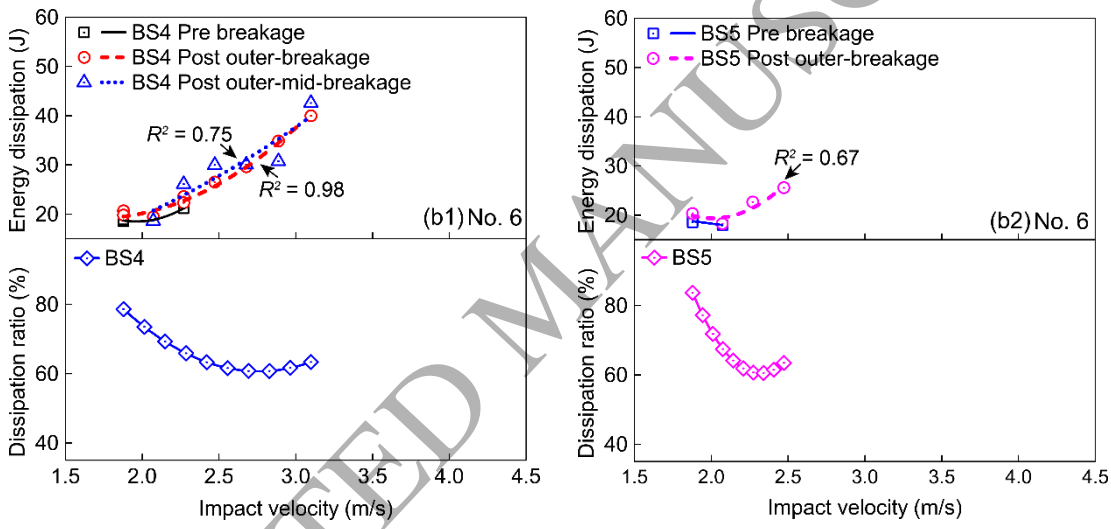

(b) No. 6 group in BS4 and BS5

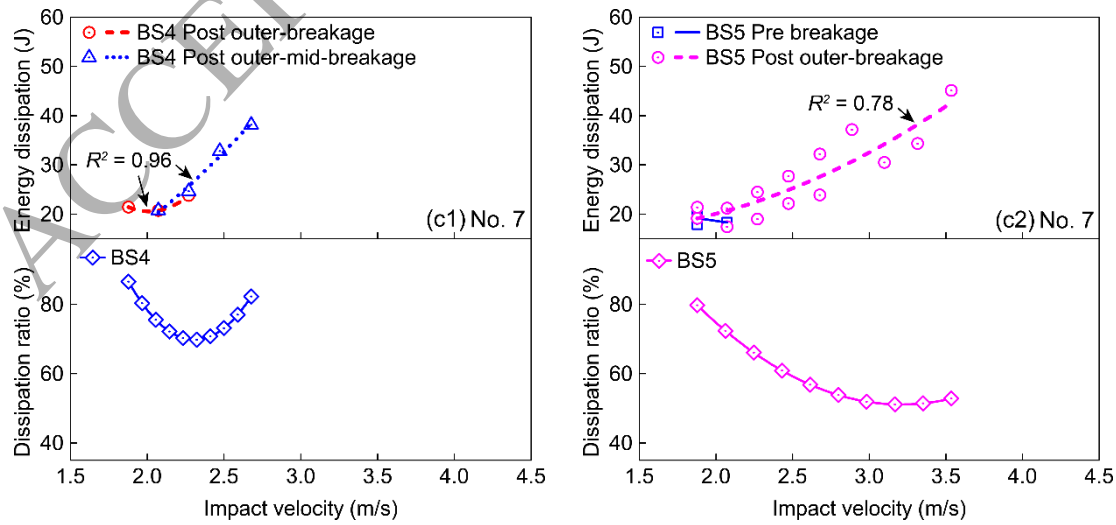

(c) No. 7 group in BS4 and BS5

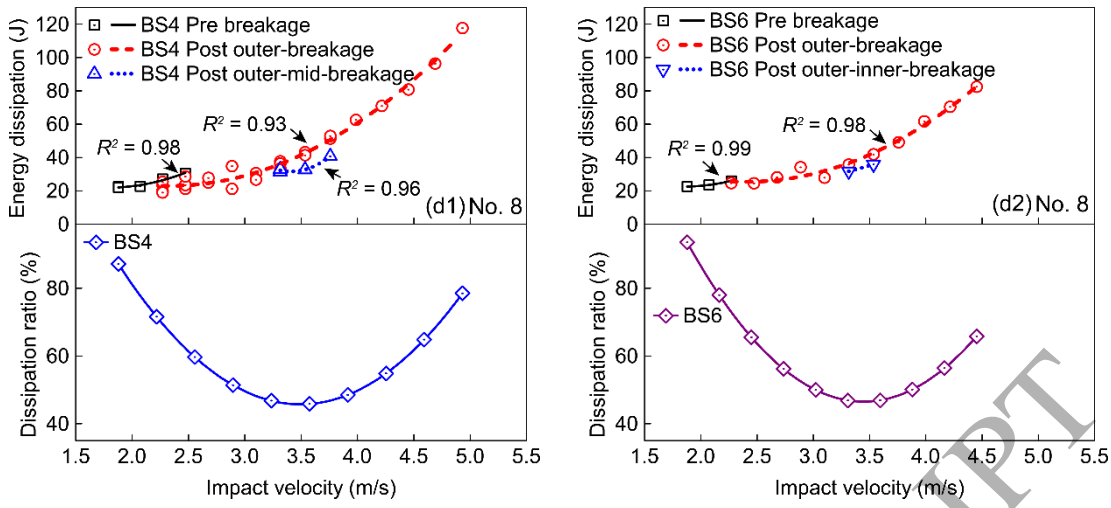

(d) No. 8 group in BS4 and BS6

Fig. 12. Impact energy dissipation and dissipation ratio variation of triple layered specimens.

3.6 Delamination

Two types of delamination pattern can be observed in the experiment: 1) delamination occurring at the outermost interface, which was frequently observed in both the double and triple layered specimens (referred to as Type I, as indicated in **Fig. 13**); and 2) delamination occurring away from the outermost interface, which can only be found in triple layered specimens (referred to as Type II, as shown in **Fig. 14**).

As shown in **Fig. 13 (a)**, a Type I delamination pattern leads to the entire detachment of fragments near the impact point in the outer glass layer. Outside the circular detaching zone, the annular shape of the partial debonding zone can be found. The entire detaching zone in the inner glass layer (**Fig. 13 (b)**), which is characterised as having sharp triangular fragments detached, is much smaller than that in the outer glass layer. Similarly a smaller partial debonding zone can be found further outwards. The entire detaching zone in the inner layer can hardly be found in all triple layered specimens because of the strong cushioning effects by the two SGP interlayers. The delamination process can also be observed from the high speed photo shown in **Fig. 13 (c)**, which agrees with the naked eye observation in **Fig. 13 (a) and (b)**.

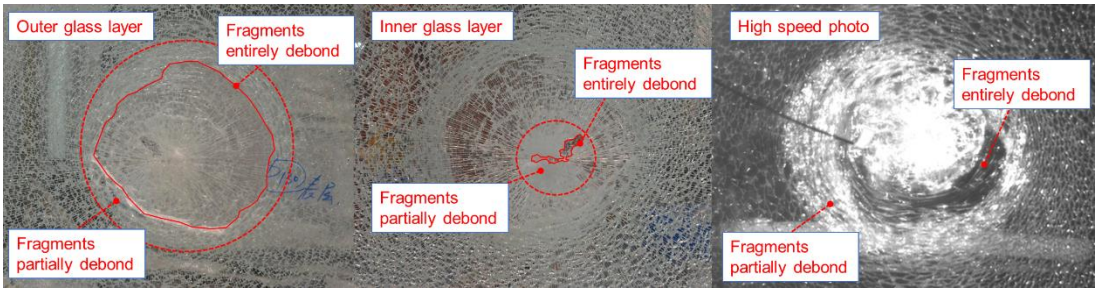

(a) Outer layer delamination (b) Inner layer delamination (c) High speed photo showing delamination

Fig. 13. Type I delamination pattern of specimen No. 1.

The Type II delamination pattern that occurs at the interfaces between the middle glass layer and both SGP interlayers can be frequently observed in the triple layered specimens, in particular, groups No. 5 and No. 8. Type I and Type II delamination zones are denoted by Disc 1 with a dot-dash line and Disc 2 with dashed line, respectively, in **Fig. 14**. Both Discs 1 and 2 in group No. 8 (**Fig. 14 (b)**), with a clamped edge, are evidently larger than those in group No. 5 (**Fig. 14 (a)**), with the bolted connection. The width of the annular zone between Disc 1 and Disc 2 is found to be similar in both groups, at 65 mm for group No. 5 and 70 mm for group No. 8.

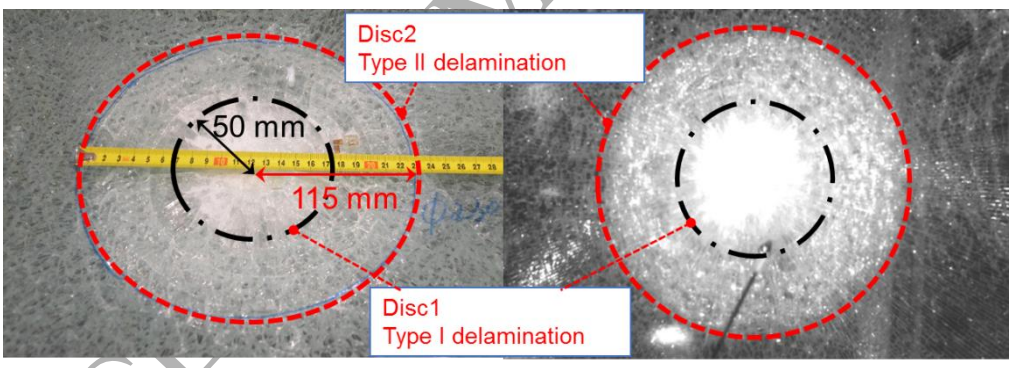

(a) Specimen No. 5 with bolted connection

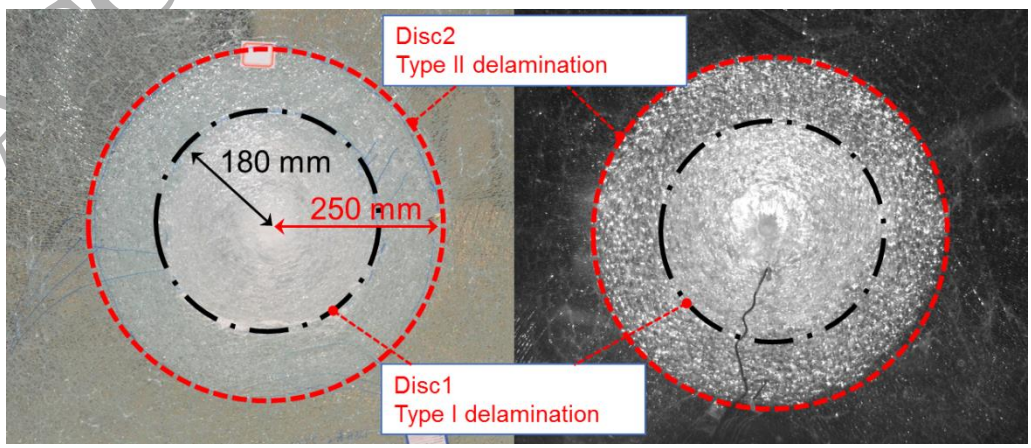

(b) Specimen No. 8 with edges clamped

Fig. 14. Type I & II delamination patterns of specimen No. 5 and No. 8.

By tracking the delamination process by analysing the high speed photos displayed in **Fig. 15**, it can be found that the most of delamination in the LG specimens with bolted connections tends to propagate at the same impact event that leads to the glass breakage. Only the minor growth of delamination can be found after such impact event. The delamination in the LG specimens with the clamped edges, on the contrary, usually occurs during the multiple impacts. The delamination growth of specimens No. 5 and No. 8 is shown in **Fig. 15**. It can be seen that the Type I delamination zone, that is Disc 1, remains almost constant after reaching a certain size; whereas the Type II delamination zone continues to grow after the subsequent impact. Type II delamination in specimen No. 8 (**Fig. 15 (b)**) occurs much earlier than in specimen No. 5 (**Fig. 15 (a)**), where Type I delamination is predominant in the early stage.

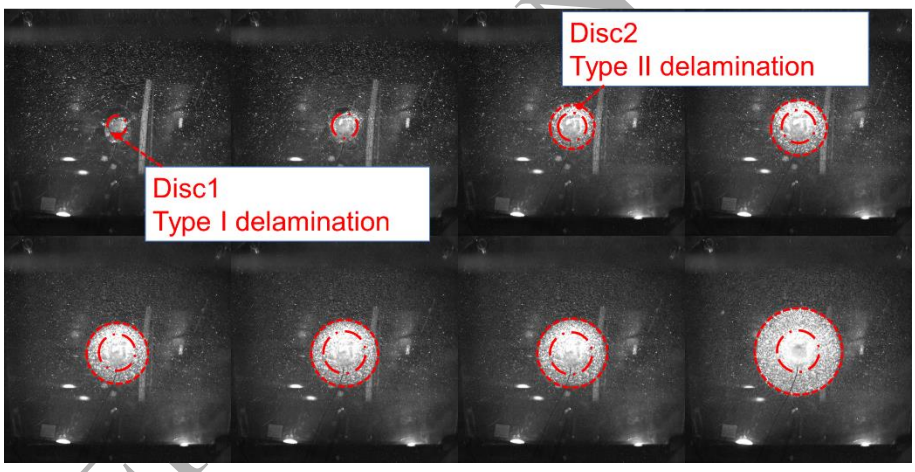

(a) Specimen No. 5 with bolted connection

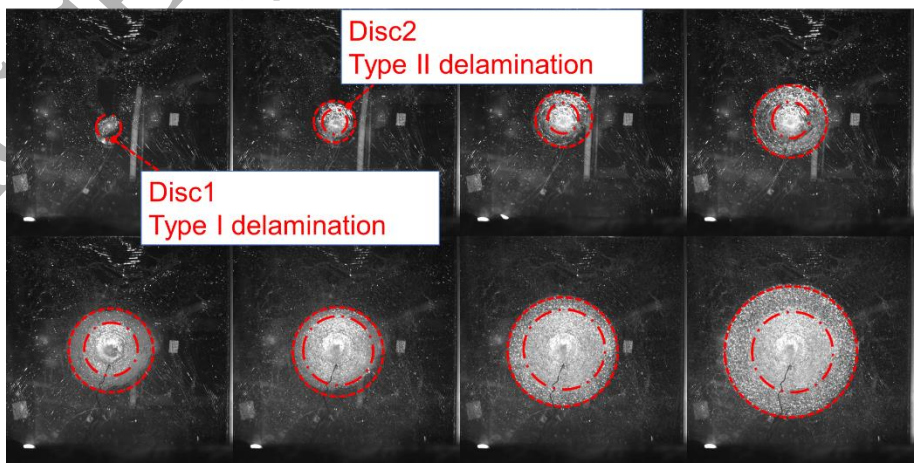

(b) Specimen No. 8 with edges clamped

Fig. 15. Delamination growth of specimen No. 5 and No. 8.

The sizes of the Disc 1 and Disc 2 delamination zones and the corresponding impact velocity of each triple layered specimen are recorded and shown in **Fig. 16**. It is worth noting that delamination in most double layered specimens is not evident, except for in specimen No. 1 that presents typical Type I delamination as shown in **Fig. 13**. The sizes of the delamination zones of the double layered specimens are therefore not considered here. It can be seen from **Fig. 16** that the specimens with bolted connections show consistent results for Disc 1 sizes from the repeated tests in the same group. The mean diameters of Disc 1 in specimens No. 5, No. 6 and No. 7 are 100 mm, 93 mm and 74 mm, respectively. The Disc 1 sizes of these three groups remain stable and independent of impact velocity in the later impact attempts. In contrast, the Disc 2 sizes of the triple layered specimens exhibit evident dependency on impact velocity, as does the Disc 1 size of specimen No. 8. The Type II delamination zone continues to grow when impact velocity increases. This dependency indicates that edge clamping or having SGP adhesion interfaces at both sides is more likely to cause continuous delamination under repeated impacts. However, the outer and inner glass fragments, which are glued with only one SGP interlayer or with a bolted connection, are less likely to debond if they are located at a certain distance from the impact point.

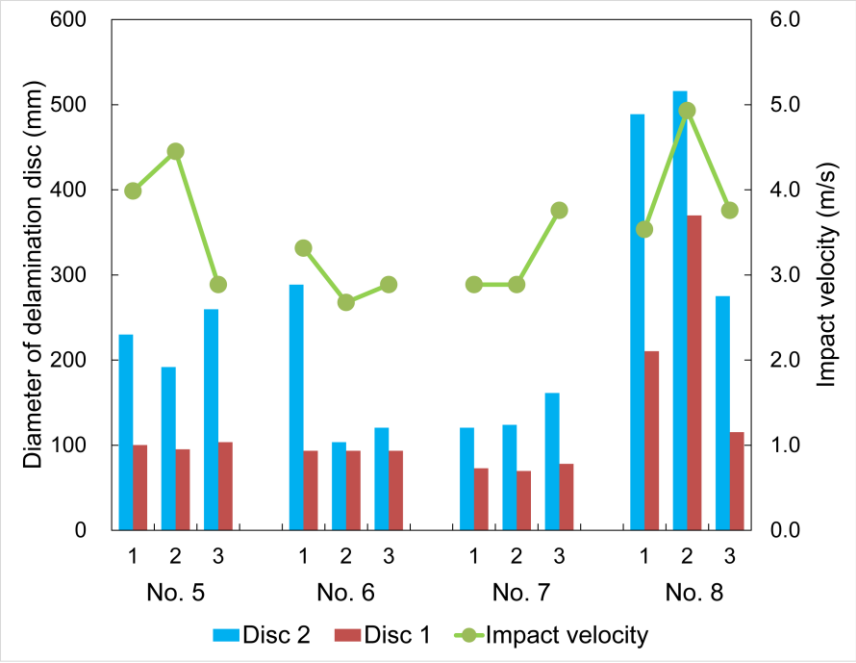

Fig. 16. Size of delamination disc of triple layered specimens.

4 Conclusions

In this paper, laboratory tests were conducted to investigate the impact damage of SGP laminated glass under the low velocity impact of a hard body. The mean minimum breakage velocity (MMBV) approach was adopted to capture the minimum energy triggering each glass breakage. This work first classifies the breakage sequences revealed by testing eight groups of SGP LG panels divided into six categories. By analysing high speed photos, the lag time between the initiation of radial cracks and rippled cracks is identified on the occasions that the glass layers break during the same impact attempt.

The effects caused by five design variables on the impact resistance of SGP LG panels were then examined. It was found that the panel size has limited effect on the breakage energy and the breakage stiffness. The impact resistance of the initial glass breakage cannot be further improved by increasing the SGP interlayer thickness. Test results show that a LG panel with a clamped edge requires a higher MMBV to trigger glass breakage, and has a higher pre-breakage stiffness than that with a bolted connection. A beneficial cracking pattern of HS glass fragments that results in the evident improvement of breakage stiffness as well as a slight increase in MMBV can be identified when the HS side receives the impact. In the case of the double layered LG with a thicker interlayer, and the triple layered LG, the dynamic stiffness yields a significant degradation in the post-breakage stage. The results also reveal that the LG panels with FT glass layers can exhibit better ‘ductility’ against impacts, in particular in those panels with clamped edges.

By examining the energy dissipation behaviour, results indicate that the energy dissipation ratio can be more than 40% on most occasions. Negative effects on dissipating impact energy are shown when SGP interlayer thickness increases. Two types of delamination patterns are observed and examined. The delamination tends to continue growing when impact velocity increases, apart from on one occasion, where outermost-interface delamination occurred in the bolted glass panel.

Acknowledgement

This work was supported by the National Key Research and Development Program of China [Grant No. 2017YFC0806100], the National Natural Science Foundation of China [Grants No.

51378308, 51508543] and the Science Research Plan of Shanghai Municipal Science and Technology Committee [Grant No. 17DZ1200306].

Reference

[1] Belis J, Depauw J, Callewaert D, Delincé D, Impe RV. Failure mechanisms and residual capacity of annealed glass/SGP laminated beams at room temperature. Engineering Failure Analysis. 2009;16(6):1866-75.

[2] Bennison SJ, Smith CA, Duser AV, Jagota A. Structural performance of laminated glass made with a "stiff" interlayer. The use of glass in buildings: ASTM International; 2002.

[3] Kaiser ND, Behr RA, Minor JE, Dharani LR, Ji F, Kremer PA. Impact Resistance of Laminated Glass Using "Sacrificial Ply" Design Concept. Journal of Architectural Engineering. 2000;6(1):24-34.

[4] Wang X-e, Yang J, Liu Q-f, Zhang Y-m, Zhao C. A comparative study of numerical modelling techniques for the fracture of brittle materials with specific reference to glass. Engineering Structures. 2017;152:493-505.

[5] Wang X-e, Yang J, Wang F, Liu Q, Xu H. Simulating the impact damage of laminated glass considering mixed mode delamination using FEM/DEM. Composite Structures. 2018. https://doi.org/10.1016/j.compstruct.2018.05.127

[6] Rooij LV, Bhalla K, Meissner M, Ivarsson J, Crandall J, Longhitano D, et al. Pedestrian crash reconstruction using multi-body modeling with geometrically detailed, validated vehicle models and advanced pedestrian injury criteria. 18th ESV Conference, 2003.

[7] Hooper PA, Sukhram RAM, Blackman BRK, Dear JP. On the blast resistance of laminated glass. International Journal of Solids & Structures. 2012;49(6):899-918.

[8] Larcher M, Solomos G, Casadei F, Gebbeken N. Experimental and numerical investigations of laminated glass subjected to blast loading. International Journal of Impact Engineering. 2012;39(1):42-50.

[9] Zhang X, Hao H, Wang Z. Experimental study of laminated glass window responses under impulsive and blast loading. International Journal of Impact Engineering. 2015;78:1-19.

[10] ASTM E1886-13a, Standard Test Method for Performance of Exterior Windows, Curtain Walls, Doors, and Impact Protective Systems Impacted by Missile(s) and Exposed to Cyclic Pressure Differentials. ASTM International; 2013.

[11] ASTM E1996-14a, Standard Specification for Performance of Exterior Windows, Curtain Walls, Doors, and Impact Protective Systems Impacted by Windborne Debris in Hurricanes. ASTM International; 2014.

[12] Knight CG, Swain MV, Chaudhri MM. Impact of small steel spheres on glass surfaces. Journal of Materials Science. 1977;12(8):1573-86.

[13] Pantelidesa CP, Horstb AD, Minorc JE. Post-breakage behavior of architectural glazing in Windstorms. Journal of Wind Engineering & Industrial Aerodynamics. 1992;44(1-3):2425-35.

[14] Zhang X, Hao H, Ma G. Laboratory test and numerical simulation of laminated glass window vulnerability to debris impact. International Journal of Impact Engineering. 2013;55(5):49-62.

[15] Grant PV, Cantwell WJ, McKenzie H, Corkhill P. The damage threshold of laminated glass structures. International Journal of Impact Engineering. 1998;21(9):737-46.

[16] Behr RA, Kremer PA, Dharani LR, Ji FS, Kaiser ND. Dynamic strains in architectural laminated glass subjected to low velocity impacts from small projectiles. Journal of Materials Science. 1999;34(23):5749-56.

[17] Saxe TJ, Behr RA, Minor JE, Kremer PA, Dharani LR. Effects of Missile Size and Glass Type on Impact Resistance of "Sacrificial Ply" Laminated Glass. Journal of Architectural Engineering. 2002;8(1):24-39.

[18] European Enhanced Vehicle-safety Committee. EEVC Working Group 17 Report - Improved Test Methods to Evaluate Pedestrian Protection Afforded by Passenger Cars. Delft, Netherlands: TN0 Crash-Sagety Research Centre, 1998.

[19] Pyttel T, Liebertz H, Cai J. Failure criterion for laminated glass under impact loading and its application in finite element simulation. International Journal of Impact Engineering. 2011;38(4):252-63.

[20] Liu B, Xu T, Xu X, Wang Y, Sun Y, Li Y. Energy absorption mechanism of polyvinyl butyral laminated windshield subjected to head impact: Experiment and numerical simulations. International Journal of Impact Engineering. 2016;90:26-36.

[21] Ivanov I, Sadowski T. Efficient finite element models of laminated glass subjected to low-velocity impact. Challenging Glass 4 & COST Action TU0905 Final Conference; Lausanne, 2014.

[22] Huang X-h, Yang J, Liu Q-f, Zhu J, Bai L, Wang F-l, et al. A simplified flange–lip model for distortional buckling of cold-formed steel channel-sections with stiffened web. International Journal of Mechanical Sciences. 2018;136:451-9.

[23] Mohagheghian I, Wang Y, Jiang L, Zhang X, Guo X, Yan Y, et al. Quasi-static bending and low velocity impact performance of monolithic and laminated glass windows employing chemically strengthened glass. European Journal of Mechanics - A/Solids. 2017;63:165-86.

[24] Louter C, Belis J, Veer F, Lebet JP. Durability of SG-laminated reinforced glass beams: Effects of temperature, thermal cycling, humidity and load-duration. Construction & Building Materials. 2012;27(1):280-92.

[25] Bedon C, Belis J, Luible A. Assessment of existing analytical models for the lateral torsional buckling analysis of PVB and SG laminated glass beams via viscoelastic simulations and experiments. Engineering Structures. 2014;60(2):52-67.

[26] Louter C, Belis J, Veer F, Lebet J-P. Structural response of SG-laminated reinforced glass beams; experimental investigations on the effects of glass type, reinforcement percentage and beam size. Engineering Structures. 2012;36(Supplement C):292-301.

[27] BS EN 356 - Glass in building. Security glazing. Testing and classification of resistance against manual attack. British Standards Institution; 2000.

[28] Xu X, Xu J, Chen J, Li P, Liu B, Li Y. Investigation of dynamic multi-cracking behavior in PVB laminated glass plates. International Journal of Impact Engineering. 2017;100:62-74.

[29] Acloque P. Déformation et rupture des verres. Ann Mines. 1975;2:57-66.

[30] Nielsen JH, Olesen JF, Stang H. The Fracture Process of Tempered Soda-Lime-Silica Glass. Experimental Mechanics. 2008;49(6):855.

[31] Molnár G, Ferentzi M, Weltsch Z, Szebényi G, Borbás L, Bojtár I. Fragmentation of wedge loaded tempered structural glass. Glass Structures & Engineering. 2016;1(2):385-94.

[32] Chen J, Xu J, Yao X, Liu B, Xu X, Zhang Y, et al. Experimental investigation on the radial and circular crack propagation of PVB laminated glass subject to dynamic out-of-plane loading. Engineering Fracture Mechanics. 2013;112-113:26-40.

[33] Dugnani R, Zednik RJ, Verghese P. Analytical model of dynamic crack evolution in tempered and strengthened glass plates. International Journal of Fracture. 2014;190(1-2):75-86.

[34] Lopes CS, Seresta O, Coquet Y, Gürdal Z, Camanho PP, Thuis B. Low-velocity impact damage on dispersed stacking sequence laminates. Part I: Experiments. Composites Science and Technology. 2009;69(7-8):926-36.

[35] Serge Abrate. Impact on composite structures: Cambridge University Press; 1998.

[36] Pelfrene J, Van Dam S, Van Paepegem W. Numerical analysis of the peel test for characterisation of interfacial debonding in laminated glass. International Journal of Adhesion and Adhesives. 2015;62:146-53.